2023-08-01

A DFT Analysis And Simple Hamiltonian Modeling Of A Molecular System Employed For Experimental Evidence Of Quantum Teleportation

Pedro Ulises Medina Gonzalez
University of Texas at El Paso

A DFT ANALYSIS AND SIMPLE HAMILTONIAN MODELING OF A MOLECULAR SYSTEM EMPLOYED FOR EXPERIMENTAL EVIDENCE OF QUANTUM TELEPORTATION

PEDRO ULISES MEDINA GONZALEZ

Master's Program in Physics

APPROVED:

Tunna Baruah, Chair, Ph.D.

Mark R. Pederson, Co-Chair, Ph.D.

Rajendra Zope, Ph.D.

Sreeprasad T. Sreenivasan, Ph.D.

Stephen L. Crites, Jr., Ph.D.
Dean of the Graduate School

to my

MOTHER and FATHER

with love

A DFT ANALYSIS AND SIMPLE HAMILTONIAN MODELING OF A MOLECULAR SYSTEM EMPLOYED FOR EXPERIMENTAL EVIDENCE OF QUANTUM TELEPORTATION

by

PEDRO ULISES MEDINA GONZALEZ, B.S.

THESIS

Presented to the Faculty of the Graduate School of

The University of Texas at El Paso

in Partial Fulfillment

of the Requirements

for the Degree of

MASTER OF SCIENCE

Department of Physics

THE UNIVERSITY OF TEXAS AT EL PASO

August 2023

Acknowledgements

I want to thank my advisor, Dr. Tunna Baruah of the Physics Department at the University of Texas at El Paso, for her advice and constant support.

I also wish to thank the other members of my committee: Dr. Mark Pederson of the Physics Department at the University of Texas at El Paso, for enriching my project through the development of the model Hamiltonian and guidance to complete it successfully. Dr. Rajendra Zope of the Physics Department at the University of Texas at El Paso for his suggestions and comments throughout the project. Lastly, Dr. Sreeprasad Sreenivasa from the Department of Chemistry and Biochemistry at the University of Texas at El Paso for his time and final input in this project.

Additionally, I want to thank my colleagues I spent my time with during my masters, the members of the electronic structure lab, and the Physics Department professors and staff for their hard work preparing me as a physicist. Lastly, I want to thank everyone who has accompanied me throughout my life for helping me become a better person, especially my father, mother, brother, and sister.

Abstract

Radical ion pairs (RIPs) have been used to demonstrate quantum teleportation in molecular systems for applications in quantum information science. Covalent organic donor-acceptor (D-A) molecules can produce RIPs through photo-induced charge transfer and an additional radical (R) molecule makes quantum teleportation possible. We present the electronic structure and analyze charge transfer excited states of a recently studied [1] D-A-R molecular system using density functional theory. The distances between donor-acceptor and donor-radical are about 12.9 Å and 21.9 Å, respectively. The excitation energies are calculated using the perturbative delta-SCF method and agree with other conventional excited-state methods and experimental reference values. Charge transfer energies change with solvent polarity, but we find that due to the ionic nature of triad, even low polarity solvents make a significant change in energies. We discuss the spin ordering energies and the Heisenberg exchange coupling parameters for this D-A-R system. Additionally, a simple Hamiltonian is modelled to work with a basis set optimized for each of the spin orbitals that are part of the spin state teleportation process.

Table of Contents

List of Tables

List of Figures

Chapter 1

Introduction

Quantum information science exploits the fundamental quantum properties of materials to achieve highly efficient computation, sensing, and secure communication. The quantum analog of bits in classical computers is called qubit that can exist as a coherent superposition of two quantum states. The qubits can be entangled with other such systems and as a result can hold large amount of information compared to classical bits. The qubits can be made up of electronic states of an atom [1], polarization states of a photon, spin states of molecule [2] or nuclei, or a current loop in a superconductor[3]. A few such examples are nitrogen vacancy in diamond [4], trapped ion [5, 6], spin states of a single molecule magnet [7], spin states of quantum dots [8], superconducting circuits [9]. For reliable quantum information processing the qubits should be such that they can be prepared in distinct initial states, should have low decoherence, allow for quantum gate operations and quantum measurements [2].

The challenges concerning the use of the qubits mentioned above are requirement of extremely low temperature, difficulties in fabricating the qubits in specific locations in solid devices, and need for isolation from environment to reduce decoherence etc. Another promising type of qubits is the molecular qubits with specified ligands and spin centers. One such type of single molecular magnet has been speculated early on [7]. Molecular magnets have high spins and can have more than two quantum states. Another type is organic light-harvesting molecules that contain a pair of electron donor and acceptor components. Such molecules have been studied widely for potential use in organic solar cell. These molecules when photoexcited undergo electron transfer from the donor to the acceptor and thereby form a radical ion pair.

Radical ion pairs we are interested in are organic bimolecular or supramolecular systems that can occur through photo-induced charge transfer reaction. These are short lived states with lifetimes of nano-seconds. In the photo-induced charge transfer reactions the electron donor and acceptor molecules form the ion pair. Assuming the ground state to be spin singlet, the charge transfer creates two unpaired spins on the donor and the acceptor sites. The system can interconvert coherently from the initial pure singlet state to triplet state due to hyperfine, Zeeman, exchange, and dipolar interactions [10]. The singlet and triplet states of the ion pair can be very close in energy depending on the separation between the donor and acceptor molecules. In systems with large separation between the electron donor and acceptor, the exchange and dipole coupling between the two unpaired spins is typically weak. The intersystem crossing in such cases is mainly driven by hyperfine coupling. The mixing of the singlet and triplet states leads to different results of chemical reactions or the recombination process when placed in a magnetic field.

The focus here is to study such a supramolecular system that lead to formation of a radical ion pair upon photo-excitation. The focus here is to study one such supramolecular system that lead to formation of a radical ion pair upon photo-excitation. The two spins on the donor and acceptor sites can form a singlet $|S\rangle$ and three triplet states $|T_0\rangle$, $|T_{+1}$, and $|T_{-1}\rangle$ states. In the absence of any magnetic field these can form four Bell states. In the presence of the large magnetic field, the singlet and the $|T_0\rangle$ and will remain close in energy whereas the other two triplet states will be too high and too low in energy compared to these two. In that case, the S and T_0 states can form two mixed states.

1.0.1 Quantum Teleportation

The molecule we are interested in is conjugated with a neutral radical to demonstrate teleportation of quantum states [11]. Quantum teleportation is transfer of an unknown quantum state over a physical distance. Quantum state teleportation was first proposed theoretically in 1993 by Bennett et al. [12]. In this thought experiment, there exists a classical and a quantum channel between the sender Alice and the receiver Bob. Alice

wants to transmit the unknown state of a spin -1/2 particle 1 to Bob. Alice also has another spin-1/2 particle 2 and Bob too has a spin-1/2 particle 3. The particles 2 and 3 are prepared in an initial singlet state

$$|\Psi_{23}^{-}\rangle = \frac{1}{\sqrt{2}}[|\uparrow_2\rangle|\downarrow_3\rangle - |\uparrow_3\rangle|\downarrow_2\rangle]$$

. Next Alice performs a Bell state measurement on the joint state of particle 1 and particle 2. The Bell states of particle 1 and 2 are:

$$|\Psi_{12}^{-}\rangle = \frac{1}{\sqrt{2}}[|\uparrow_1\rangle|\downarrow_2\rangle - |\uparrow_2\rangle|\downarrow_1\rangle]$$

.

$$|\Psi_{12}^{+}\rangle = \frac{1}{\sqrt{2}}[|\uparrow_1\rangle|\downarrow_2\rangle + |\uparrow_2\rangle|\downarrow_1\rangle]$$

.

$$|\Phi_{12}^{-}\rangle = \frac{1}{\sqrt{2}}[|\uparrow_1\rangle|\uparrow_2\rangle - |\downarrow_2\rangle|\downarrow_1\rangle]$$

.

$$|\Phi_{12}^{+}\rangle = \frac{1}{\sqrt{2}}[|\uparrow_1\rangle|\uparrow_2\rangle + |\downarrow_2\rangle|\downarrow_1\rangle]$$

. The unknown state $|\phi_1 >= a|\uparrow_1\rangle + b|\downarrow_1\rangle$ where $a^2 + b^2 = 1$.

Before the measurement the complete state of the three particles is then

$$|\Psi_{123}\rangle = \frac{a}{\sqrt{2}}|\uparrow_1\rangle[|\uparrow_2\rangle|\downarrow_3\rangle - |\uparrow_2\rangle|\downarrow_3\rangle] + \frac{b}{\sqrt{2}}|\downarrow_1\rangle[|\uparrow_2\rangle|\downarrow_3\rangle - |\uparrow_2\rangle|\downarrow_3\rangle].$$

The product states of particle 1 and 2 can be written in term of $\Psi_{12}^{\pm}\rangle$ and $|\Phi_{12}^{\pm}\rangle$. For example,

$$|\uparrow_1\rangle|\downarrow_2\rangle = \frac{1}{\sqrt{2}}[\Psi_{12}^{-} + \Psi_{12}^{+}].$$

This leads to

$$|\Psi_{123}\rangle = \frac{1}{2}[|\Psi_{12}^{-}\rangle(-a|\uparrow_3\rangle - b|\downarrow_3\rangle) + |\Psi_{12}^{+}\rangle(-a\uparrow_3\rangle + b|\downarrow_3\rangle) + |\Phi_{12}^{-}\rangle(a|\downarrow_3\rangle + b|\uparrow_3\rangle) + |\Phi_{12}^{+}\rangle(a\downarrow_3\rangle - b|\uparrow_3\rangle)]$$

. The probability of the four measurement results are same. After measurement, particle 3 will be projected into one of the four pure states which can be written as

$$|\phi_3\rangle = \begin{pmatrix} -1 & 0 \\ 0 & -1 \end{pmatrix}\begin{pmatrix} a \\ b \end{pmatrix}, \begin{pmatrix} -1 & 0 \\ 0 & 1 \end{pmatrix}\begin{pmatrix} a \\ b \end{pmatrix}, \begin{pmatrix} 0 & 1 \\ 1 & 0 \end{pmatrix}\begin{pmatrix} a \\ b \end{pmatrix}, \begin{pmatrix} 0 & -1 \\ 1 & 0 \end{pmatrix}\begin{pmatrix} a \\ b \end{pmatrix}.$$

Each of the particle 3's state is related to the state $|\phi_1\rangle$ of particle 1. Depending on the outcome of the measurement which Alice sends to Bob through the classical channel, Bob can replicate the state of particle 1 on 3. In case of the singlet outcome $|\Psi_{12}^{-}\rangle$, then particle 3 is in the same state except for a phase factor. In case of the other three outcomes, Bob will need to use one of the unitary operators to replicate the state of particle 1.

Quantum teleportation was been demonstrated experimentally in 1997 [13, 14] and has been extended to many different types of quantum systems such as including photonic qubits [15, 16, 17, 18], nuclear magnetic resonance [19], optical modes[20, 21]atomic ensembles [22, 23] trapped atoms [23]and solid-state systems [24]. A detailed description of the different types of teleportation experiments can be found in Refs. [25, 26].

1.0.2 Radical-Ion-Pair based molecule for quantum teleportation

The method of using radical ion pair for spin state teleportation was put forward by Sakikhov et al. [27] in 2007. In this scheme a single spin carrying unit A^- is prepared in an initial state. Another two components B and C form the electron donor and acceptor pair when photoexcited. Photoexcitation and charge transfer lead to the formation of the $B^+ - C^-$ ion pair. The recombination of $(A^- - B^+)$ leads to the formation of $(A - B)C^-$ state in which the original spin state on A is transmitted to the C component. The recombination is equivalent to the Bell measurement step.

The radical pair molecule that was used for spin state teleportation was synthesized and studied by Wasielewsky et al. in 2018 [11] in which donor is 2,2,6,6-tetramethylbenzo[1,2-d:4,5-d']bis([1,3]dioxole), acceptor is 4-aminonaphthalene-1,8-imide and a radical which is equivalent to the spin carrying component A mentioend above. The radical used was a partially deuterated α, γ-bisdiphenylene-β-phenylallyl also known as Koelsch radical. The radical was prepared in an initial state with its spin perpendicular to an external magnetic field. Next the D-A complex was photoexcited to form the $D^+ - A^- - R$. A charge transfer from A^- to the R forms the $D^+ - A - R^-$ state in which the initial spin state on R is teleported to the D^+ component over a distance of 2 nm. The charge transfer from A^- to

R constitutes the Bell state measurement step.

To be able to be used as a qubit, the quantum behavior should persist even in the presence of the environment. The vibrations of the molecule and coupling to the environment should not negatively affect its performance. In this work we study the electronic structure of the $D - A - R$ complex, its excited states, and develop a simplified model to study the quantum behavior of such systems. The chapters of this thesis are organized as follows. In chapter 2, the methods for calculation of various properties are described. The results on the electronic structure and excited states are included in Chapter 3 and the details on the calculation of the parameters for the model are given in chapter 4. The future work is given in chapter 5.

Chapter 2

Theoretical Background

To study the properties of the radical-ion-pair, we used density functional theory (DFT) for our calculations. In the following we give a brief description of the fundamental ideas related to electronic structure calculations and to DFT. [28, 29, 30, 31]. We start with the Schrodinger equation to describe the motion of a many-body quantum system and brifly describe the commonly used approximations and principles such as Born-Oppenheimer approximation to focus on the electronic structure of the system, the variational principle as the primary tool to obtain the ground state energy of any system, the Slater determinantal form of the wave function that follows the antisymmetry principle of electrons. Before explaining DFT, we have the Hartree-Fock method, an analogous method to DFT that uses the electron's wave function instead. We introduce DFT, from the Hohenberg-Kohn theorems and Kohn-sham equations, to the exchange-correlation approximations. Finally, We discuss excited state methods to study more properties.

2.1 Density Functional Theory

Several computational modeling methods exist to study the electronic structure of many-body systems. Density functional theory (DFT) is a powerful tool for calculating the electron properties of atoms and molecules considering their quantum behavior. A balance between accuracy and computational cost makes DFT regularly used for practical problems in physics, chemistry, material science, and other disciplines. We will see that the main advantage of DFT over other methods is the simplification of the N interacting electrons problem to an equivalent one of N noninteracting electrons in an effective potential.

2.1.1 Atomic Units

Before we begin, there is a necessary clarification. This manuscript uses atomic units in which the following fundamental constants are set to unity

$$\hbar = e = a_0 = m_e = 1, \tag{2.1}$$

where $\hbar$ is the reduced Planck's constant, e is the electron's charge, a_0 is the Borh radius, and m_e is the mass of the electron. The atomic unit of energy and length are Hartree and Bohr, respectively.

2.1.2 Schrodinger Equation

The essential differential equation to study a particle in the realm of (nonrelativistic) quantum mechanics is Schrodinger's equation

$$\hat{H} \left|\Psi\right\rangle = -\imath\hbar \frac{\partial}{\partial t} \left|\Psi\right\rangle . \tag{2.2}$$

$\left|\Psi\right\rangle$ is the quantum state of a wave function, the mathematical object that represents a particle. The Hamiltonian $\hat{H}$ acts on the quantum states and reproduces their evolution over time. However, we are only interested in stationary states, so we start with the time-independent Schrodinger equation

$$\hat{H} \left|\Psi\right\rangle = E \left|\Psi\right\rangle , \tag{2.3}$$

where $\hat{H}$ is now equivalent to the particle's total energy. We can expand this problem to a Hamiltonian for a system conformed of interacting M nuclei and N electrons, described by position vectors $\mathbf{R}_A$ and $\mathbf{r}_i$, respectively. The distance between Ath and Bth nucleus is $R_{AB} = |\mathbf{R}_A - \mathbf{R}_B|$; the distance between the ith and jth electron is $r_{ij} = |\mathbf{r}_i - \mathbf{r}_j|$, and the distance between the ith electron and Ath nucleus is $r_{iA} = |\mathbf{r}_i - \mathbf{r}_A|$. Therefore, the

Hamiltonian for interacting M nuclei and N electrons is

$$\begin{aligned}\hat{H} &= -\sum_{i}^{N}\frac{\nabla_i^2}{2m_e} - \sum_{A}^{M}\frac{\nabla_A^2}{2m_A} + \frac{1}{2}\sum_{A\neq B}^{M}\frac{Z_A Z_B}{R_{AB}} + \frac{1}{2}\sum_{i\neq j}^{N}\frac{e^2}{r_{ij}} - \sum_{i,A}^{N,M}\frac{eZ_A}{r_{iA}} \\ &= T_e + T_n + V_{nn} + V_{ee} + V_{en}. \end{aligned} \tag{2.4}$$

The first two terms are the electron and nuclear kinetic energy, respectively. The third and fourth terms are the repulsive interaction between nuclei and between electrons (coulomb repulsion). The last term is the attractive interaction between electrons and nuclei. Likewise, a new wave function will depend on the coordinates of all electrons and nuclei

$$\Psi = \Psi(\mathbf{r}_1, \ldots, \mathbf{r}_N; \mathbf{R}_1, \ldots, \mathbf{R}_M). \tag{2.5}$$

This new equation contains $6(N + M)$ degrees of freedom, making it harder to solve the bigger our system becomes.

2.1.3 The Born-Oppenheimer Approximation

Since the nuclei are heavier than the electrons, their motion is negligible in comparison. Using this assumption, we neglect the kinetic energy of the nuclei T_n. Moreover, we consider the electrons moving in a field of fixed nuclei to set the nuclear-nuclear repulsion potential V_{nn} constant. The remaining terms are called electronic Hamiltonian

$$\hat{H}_{electronic} = T_e + V_{ee} + V_{en}. \tag{2.6}$$

This procedure is the so-called Born-Oppenheimer approximation, where we separate our Hamiltonian's nuclear and electronic terms. To solve Schrodinger's equation with this new Hamiltonian, we also assume the total wave function to be separable into the product of electronic and nuclear wave functions

$$\Psi = \Psi_{electronic} \times \Psi_{nuclear}. \tag{2.7}$$

As a result, we obtain the many-electron Schrodinger equation

$$\hat{H}_{electronic} \left|\Psi_{electronic}\right\rangle = E_{electronic} \left|\Psi_{electronic}\right\rangle. \tag{2.8}$$

The total energy is the electronic energy $E_{electronic}$ plus the energy of the nuclear-nuclear repulsion E_{nn}. It is important to note that the motion of the electrons depends explicitly on their coordinates but also parametrically on the nuclear coordinates.

2.1.4 Variational Principle

Even after the Born-Oppenheimer approximation, the exact solutions are not available. The variational method is suitable for finding the ground state energy of this type of problems. We start with a trial wave function $\tilde{\Psi}$, which aims to be the true ground state wave function Ψ_0. Then, we define the energy as

$$E\left[\tilde{\Psi}\right] = \frac{\left\langle \tilde{\Psi} \middle| H \middle| \tilde{\Psi} \right\rangle}{\left\langle \tilde{\Psi} \mid \tilde{\Psi} \right\rangle}, \tag{2.9}$$

where we consider the possibility of a not normalized wave function. The variational principle states

$$E\left[\tilde{\Psi}\right] \geq E_0, \tag{2.10}$$

which means the calculated energy is always greater or equal to the ground state energy. Moreover, the trial wave function corresponds to the ground state wave function if the energy calculated equals the ground state energy

$$E = E_0 \Longleftrightarrow \left|\tilde{\Psi}\right\rangle = |\Psi_0\rangle\,. \tag{2.11}$$

Therefore, we can minimize the energy with respect to the trial wave function to find the ground state energy. In other words, we will eventually obtain the ground state energy E_0 by attempting different trial wave functions.

2.1.5 Antisymmetry Principle, Hartree Product, and Slater Determinant

The wave function we have shown depends only on the spatial coordinates of the electrons. However, another variable that we need to include is the spin coordinate. If we have one

particle in terms of spatial coordinates, we call it spatial orbital $\psi(\mathbf{r})$. However, if we include the spin $\alpha(\omega)$, we call it a spin-orbital

$$\chi(\mathbf{x}) = \psi(\mathbf{r})\,\alpha(\omega) \;or\; \psi(\mathbf{r})\,\beta(\omega)\,. \tag{2.12}$$

The most trivial way to construct the total wave function is a simple product of spin orbitals for each electron

$$\Psi^{HP}(\mathbf{x}_1, \mathbf{x}_2, \ldots, \mathbf{x}_N) = \chi_i(\mathbf{x}_1)\,\chi_j(\mathbf{x}_2)\cdots\chi_k(\mathbf{x}_N)\,. \tag{2.13}$$

This many-electron wave function is termed a Hartree product. The only problem with this approach is that it does not satisfy the following requirement: A many-electron wave function must be antisymmetric with respect to the interchange of the coordinate x(both space and spin) of any two electrons

$$\Psi(\mathbf{x}_1, \ldots, \mathbf{x}_i, \ldots, \mathbf{x}_j, \ldots, \mathbf{x}_N) = -\Psi(\mathbf{x}_1, \ldots, \mathbf{x}_j, \ldots, \mathbf{x}_i, \ldots, \mathbf{x}_N)\,. \tag{2.14}$$

This requirement is often called the antisymmetry principle. Fortunately, one can obtain antisymmetrized wave functions using the appropriate combination of Hartree products. Thus For an N-electron system, we have the following wave function:

$$\Psi(\mathbf{x}_1, \mathbf{x}_2, \ldots, \mathbf{x}_N) = \frac{1}{\sqrt{N}} \begin{vmatrix} \chi_1(\mathbf{x}_1) & \chi_2(\mathbf{x}_1) & \ldots & \chi_N(\mathbf{x}_1) \\ \chi_1(\mathbf{x}_2) & \chi_2(\mathbf{x}_2) & \ldots & \chi_N(\mathbf{x}_2) \\ \vdots & \vdots & \ddots & \vdots \\ \chi_1(\mathbf{x}_N) & \chi_2(\mathbf{x}_N) & \ldots & \chi_N(\mathbf{x}_N) \end{vmatrix} \equiv |\chi_1, \chi_2, \ldots, \chi_N\rangle\,, \tag{2.15}$$

also called slater determinant. The factor outside the determinant is a normalization factor. Moreover, each column contains the ith spin-orbital, and the rows contain the N electrons. If two electrons occupy the same orbital, we have two equal columns, making the determinant zero. Thus no more than one electron can occupy a spin-orbital (Pauli exclusion principle).

2.1.6 Hartree-Fock Method

Finally, to solve the many-electron problem, we assume that the N-electron wavefunction is equal to a single slater determinant. In this way, the system's energy depends on a set of

spin orbitals. Following the variational principle, we obtain the ground state of our system by finding the best spin orbitals that minimize the electronic energy. Recalling the terms of the electronic Hamiltonian in equation 2.6, we write the energy as

$$E_0\left[\Psi_0\right] = \left\langle \Psi_0 \right| H_{electronic} \left| \Psi_0 \right\rangle = \sum_a^N \left\langle a \right| h_a \left| a \right\rangle + \frac{1}{2} \sum_{a,b}^N \left\langle ab \right| \left| ab \right\rangle \tag{2.16}$$

$$= \sum_a^N \left\langle a \right| h_a \left| a \right\rangle + \frac{1}{2} \sum_{a,b}^N \left(\left[aa \mid bb \right] - \left[ab \mid ba \right] \right),$$

where we change the notation from $|\chi_a\rangle$ to $|a\rangle$ for more clarity. We introduce the core Hamiltonian

$$h_a = -\frac{\nabla_a^2}{2} - \sum_A^M \frac{Z_A}{r_{aA}}, \tag{2.17}$$

which defines the kinetic energy of the ath electron and the nuclear-electron attraction potential of the ath electron to the nuclei. The two terms from equation 2.16 involving sums over b correspond to the electron-electron interactions. The first one is called the coulomb term

$$\left[aa \mid bb \right] \equiv \iint d\mathbf{x}_1 d\mathbf{x}_2 \chi_a^* \left(\mathbf{x}_1 \right) \chi_a \left(\mathbf{x}_1 \right) \frac{1}{r_{12}} \chi_b^* \left(\mathbf{x}_2 \right) \chi_b \left(\mathbf{x}_2 \right). \tag{2.18}$$

It represents the average electron repulsion energy an electron in a given orbital would feel from an electron in a different orbital. The second one is called the exchange term

$$\left[ab \mid ba \right] \equiv \iint d\mathbf{x}_1 d\mathbf{x}_2 \chi_a^* \left(\mathbf{x}_1 \right) \chi_b \left(\mathbf{x}_1 \right) \frac{1}{r_{12}} \chi_b^* \left(\mathbf{x}_2 \right) \chi_a \left(\mathbf{x}_2 \right), \tag{2.19}$$

which does not have a physical representation but prevents overcounting electron-electron energy due to the antisymmetry principle. Once we minimize the energy by varying the spin-orbital restricted to their orthogonality $\langle \chi_a | \chi_b \rangle = \delta_{ab}$ and eliminate the restricted summation over $b = /a$, we retrieve the set of N Hartree-Fock equations

$$f \left| \chi_a \right\rangle = \epsilon_a \left| \chi_a \right\rangle, \tag{2.20}$$

where we define the Fock operator

$$f \equiv h_a + v_a^{HF}, \tag{2.21}$$

which is the sum of the core Hamiltonian eq.(2.17) and an effective one-electron potential called the Hartree-Fock potential

$$v_a^{HF} = \sum_b \left([aa \mid bb] - [ab \mid ba] \right). \tag{2.22}$$

In principle, the Hartree-Fock equation is an eigenvalue problem, but we often deal with wave functions written as a linear combination of atomic orbitals and, as we notice in equation 2.18 and 2.19, the coulomb and exchange terms depend on the orbitals, which means they depend on the coefficients of the linear combination, making equation 2.20 transcendental. We treat this problem using the self-consistency field (SCF) method, where we first solve for a trial set of orbitals without electron-electron interactions and then solve the original problem iteratively.

The Hartree-Fock method is not the best in electronic structure as it has some critical problems, such as the lack of correlations between electrons as it considers a single Slater determinant. Furthermore, errors arise due to the approximation of the coulomb interaction, as we consider only the interaction between an electron and the average electron distribution.

2.1.7 DFT over Hartree-Fock

Once we calculate the many-electron wavefunction, we can obtain all the information from our system. However, we sometimes want to know only the total ground state energy of the system and its changes. In this manner, Hohenberg and Kohn proposed that the energy can be defined depending only on the electron density of the system. This idea is powerful since it deals with most of the critical problems of the Hartree-Fock method. There is less computational work because the problem reduces to 3 spatial coordinates and a single spin coordinate. Moreover, the electron density is physically observable, making it easier to think about and relate to experiments. These advantages produced by the possibility of replacing the many-electron wave function with the electron density give rise to density functional theory.

2.1.8 Honenberg-kohn Theorems

Density functional theory originates from two theorems proposed and proved by Honenberg and Kohn in 1964. The first theorem states: "The ground state energy from Schrodinger's equation is a unique functional of the electron density."As mentioned in the previous section, this theorem indicates a direct relation between the ground state wave function and electron density. In this manner, we can write the energy as

$$E\left[n_0(\mathbf{r})\right] = T_e\left[n_0(\mathbf{r})\right] + V_{ee}\left[n_0(\mathbf{r})\right] + V_{en}\left[n_0(\mathbf{r})\right] = V_{en}\left[n_0(\mathbf{r})\right] + F\left[n_0(\mathbf{r})\right], \tag{2.23}$$

where we can calculate the electron-nuclear interaction energy V_{en} the same way we did for Hartree-Fock. Unfortunately, the first theorem proves the existence of a functional but says nothing about the actual expression of the functional, which we represent with the unknown $F\left[n_0(\mathbf{r})\right]$. Besides, this theorem is why we call this area density functional theory, as the energy depends on a function (electron density) instead of a value.

The second theorem proves we can apply the variational principle in DFT: "The electron density that minimizes the energy of the overall functional is the true electron density corresponding to the full solution of the Schrodinger equation."The same way we had for Hartree-Fock, but now using the electron density

$$E_0 \leq E\left[n(\mathbf{r})\right], \tag{2.24}$$

and

$$E\left[n(\mathbf{r})\right] = E_0 \Longleftrightarrow n(\mathbf{r}) = n_0(\mathbf{r}). \tag{2.25}$$

The calculated energy is always greater or equal to the ground state energy. Moreover, the trial electron density corresponds to the actual electron density if the energy calculated equals the ground state energy.

2.1.9 Kohn-sham Equations

One year after the publication of the Hohenberg-Kohn theorems, Kohn and Sham formulated a set of equations to calculate said energy functional. We start with a noninteracting

electron system feeling an external potential. The Hamiltonian of the problem is

$$H_{ref} = \sum_{i}^{N} \left(-\frac{\nabla_i^2}{2} + V_{ref}\left(\mathbf{r_i}\right) \right). \tag{2.26}$$

Then, we can rewrite the energy functional (1.23) as the kinetic energy and external potential of the noninteracting system plus the deviations from the actual system

$$E\left[n(\mathbf{r})\right] = T_{ref}\left[n(\mathbf{r})\right] + V_{en}\left[n(\mathbf{r})\right] + U\left[n(\mathbf{r})\right] + E_{XC}\left[n(\mathbf{r})\right]. \tag{2.27}$$

For the case of the external potential, we end up with nuclear-electron interaction energy V_{en}, the classical coulomb repulsion between electrons U plus a new term E_{XC} that dumps all the remains effects from the real system, such as the electron correlations, electron exchange, and the deviation of the kinetic energy. However, it is too good to be true as the exact expression for this functional is yet to be derived, and a significant part of DFT research is focused on making approximations using ab initio calculations or with experimental parameters. To begin with the minimization of the energy, we need to define the trial electron density, which is given by

$$n(\mathbf{r}) = n_{ref}(\mathbf{r}) = \sum_{i}^{N} \left|\psi_i^{KS}(\mathbf{r})\right|^2, \tag{2.28}$$

which is the sum of all probabilities of finding each electron at a given position. The Kohn-Sham wave function ψ_i^{KS} differs from the one used in the Hartree-Fock method, as it depends only on the three spatial variables of the electron density. Kohn and Sham identified that once we minimize the system's energy (maintaining orthogonality between orbitals), we can express the resulting set of equations so that each depends on a single electron. Thus, obtaining the Kohn-Sham equations

$$\left(-\frac{\nabla^2}{2} + V_{eff}\left(\mathbf{r}\right) \right) \psi_i^{KS}\left(\mathbf{r}\right) = \epsilon_i \psi_i^{KS}\left(\mathbf{r}\right). \tag{2.29}$$

Like the Hartree-Fock method, we have a set of nonlinear equations to solve using a self-consistency field process. However, the equation describes the motion of noninteracting electrons in an effective field

$$V_{eff}\left(\mathbf{r}\right) \equiv V_{en}\left(\mathbf{r}\right) + V_H\left(\mathbf{r}\right) + V_{XC}\left(\mathbf{r}\right), \tag{2.30}$$

where V_{en} is the nuclear-electron interaction potential, V_H is the Hartree potential which describes the classical coulomb repulsion between electrons

$$V_H(\mathbf{r}) = \int \frac{n(\mathbf{r}')}{|\mathbf{r} - \mathbf{r}'|} d^3r'. \tag{2.31}$$

Due to the nature of this potential, the electrons interact with themselves and generate what is known as the self-interaction error. V_{XC} is the functional derivative of the exchange-correlation energy E_{XC}

$$V_{XC}(\mathbf{r}) = \frac{\delta E_{XC}(r)}{\delta n(\mathbf{r})}. \tag{2.32}$$

Hartree-Fock approximates the coulomb energy of the electron-electron interaction and reproduces the exact exchange energy, disregarding the correlation of electrons. Meanwhile, DFT is an exact theory but produces approximated results due to the undefined exchange-correlation functional. However, DFT has the edge over Hartree-Fock on Energetic related properties considering the computational speed up provided by the electron density.

2.1.10 Exchange-Correlation Approximations

As mentioned in the previous section, the main problem in DFT is specifying the exchange-correlation functional. There are approximated functionals by optimizing parameters using experimental data but only work for the same type of system used in the experiment. Researchers also use ab initio methods to derive this functional but always use some approximation to achieve valuable results. One of the most straightforward cases to define the exchange-correlation functional is considering the uniform electron gas (UEG). In this case, the electron density is constant at all points in space, so V_{XC} is just the exchange-correlation energy of the UEG (ϵ_{XC}^{UEG}) at the electron density observed in a specific position

$$V_{XC}^{LDA}(\mathbf{r}) = V_{XC}^{LDA}(n(\mathbf{r})) = \epsilon_{XC}^{UEG}(n(\mathbf{r})). \tag{2.33}$$

This approximation uses the local density to define the approximate exchange-correlation functional, called local density approximation (LDA). Moreover, we can separate the exchange

and correlation energies

$$\epsilon_{XC}^{UEG} = \epsilon_{X}^{UEG} + \epsilon_{C}^{UEG}, \tag{2.34}$$

where we have an analytical expression for the exchange term

$$\epsilon_{X}^{UEG}(n(\mathbf{r})) = -\frac{3}{4}(\frac{3}{\pi})^{\frac{1}{3}} n(\mathbf{r})^{\frac{1}{3}}. \tag{2.35}$$

However, the correlation term is more difficult to obtain, so we must rely on stochastic numerical methods' results [32, 33, 34, 35].

Lastly, LDA works for homogeneous systems, but when the electron density varies significantly, we have less accurate results. We include the density gradient to the LDA functional to solve this problem. In such a manner, we obtain the generalized-gradient approximation (GGA) functional. Moreover, some functionals follow the same approach as the previous ones but have minor changes to increase accuracy. For example, the widely known Perdew-Burke-Ernzerhof (PBE) functional is based on this method but adds an enhancement factor.

2.2 Time-Dependent Density Functional Theory

As mentioned before, we are interested in studying the excited state properties of our molecule. Therefore, to accomplish this task, we use the extension of DFT for excited states, time-dependent density functional theory (TDDFT). As the name of the method suggests, TDDFT describes the behavior of the electrons over time, which grants tons of information in phenomena where we have a perturbation in the electrons over time, such as the presence of an electric field to create an excited state in a given system. In this section, we will review the fundamental ideas of TDDFT and a practical method [36, 37]. We keep the atomic units convention from section 2.1.1.

2.2.1 Time-dependent Schrodinger equation

For ground-state calculations, we solve the stationary time-independent Schrodinger equation 2.3. Then, for excited state calculations, we need to solve the time-dependent Schrodinger equation 2.2, which we show again with the electronic terms from Hamiltonian 2.4 for visibility,

$$\hat{H}(t)\left|\Psi(t)\right\rangle = \imath\frac{\partial}{\partial t}\left|\Psi(t)\right\rangle,\ \hat{H}(t) = T_e + V_{ee} + V_{ext}(t). \tag{2.36}$$

Now we have an initial wavefunction $\Psi(t)$ and a time-dependent external potential. This external potential depends on the nuclear-electron interaction V_{en} with the position of the nucleus changing in time and N number of fields applied to the system (e.g., electric field).

$$V_{ext}(t) = V_{en}(t) + \sum_{i}^{N} v_{ext}(r_i, t). \tag{2.37}$$

If solving eq.(2.2) is already hard, adding the time dependency makes solving eq.(2.36) much harder. However, we will see that a theorem inspired by the Hohenberg-kohn theorems simplifies our problem and gives rise to TDDFT.

2.2.2 Runge-Gross Theorem

Time-Dependent Density Functional Theory originates from a theorem proposed and proven by Erich Runge and Eberhard K. U. Gross in 1984. The theorem states that there is a one-to-one correspondence between the external potential $V_{ext}(t)$ and the density $n(r,t)$ of the system evolving from an initial state $\Psi(t)$. Schematically, we have

$$\Psi(t) : v_{ext} \longleftrightarrow n. \tag{2.38}$$

For the backward arrow, a time-dependent density indicates a single external potential for a given initial state. In other words, two different potentials correspond to two different densities for a given initial state. The forward arrow represents the unique solution of the Schrodinger equation. Then, the wavefunction is a functional of the density and initial

state and differs up to a purely-time-dependent phase,

$$\Psi(t) = e^{-\imath\alpha(t)}\Psi[n,\Psi_0](t). \tag{2.39}$$

The first Hohenberg-kohn theorem states that the energy of the ground state is a unique functional of the system's density. In this case, the expectation value of any quantum Hermitian operator is a unique functional of the time-dependent density and the initial state,

$$Q[n,\Psi_0](t) = \left\langle \Psi[n,\Psi_0](t) \left| \hat{Q}(t) \right| \Psi[n,\Psi_0](t) \right\rangle. \tag{2.40}$$

2.2.3 Time-Dependent Kohn-Sham Equations

Similar to the ground state case, we use a Kohn-Sham system (fictitious noninteracting system of fermions) to solve our time-dependent problem. Therefore, we can write the time-dependent Kohn-Sham equations with orbitals $\varphi_j(r,t)$ as,

$$\imath\frac{\partial}{\partial t}\varphi_j(r,t) = [-\frac{\nabla^2}{2} + v_{KS}[n;\Phi_0](r,t)]\varphi_j(r,t), \tag{2.41}$$

whose density,

$$n(r,t) = \sum_{j=1}^{N} |\varphi_j(r,t)|^2 \tag{2.42}$$

Is that of the real system. As mentioned in the previous section, a unique density corresponds to the KS potential. Akin to the ground state problem, we divide the KS potential into three terms,

$$v_{KS}[n;\Phi_0](r,t) = v_{ext}[n;\Psi_0](r,t) + \int d^3r' \frac{n(r',t)}{|r-r'|} + v_{xc}[n,\Psi_0,\Phi_0](r,t), \tag{2.43}$$

where the first term is the external potential that depends on the initial state and the density. The second term is the classical interaction between electrons, the Hartree potential with time dependency. The last term is the typical exchange-correlation potential that we need to approximate, but more complex as it depends on the whole history of density (creating memory problems), the initial interacting wavefunction Ψ_0, and the initial Kohn-sham wavefunction Φ_0 which is almost always a single Slater determinant.

To extract the excited state energies of a system, we solve TDKS equations 2.41by calculating the time evolution operator of the system and propagating the equations for some time until we find a certain number of poles that correspond to the excited state energies. However, to extract the energies of low-lying excited states (excited state property studied in this manuscript), there is a method that does not use TDKS equations but instead uses perturbation theory and TDDFT formalism.

2.2.4 TDDFT in linear response

As always, constructing the exchange-correlation potential V_{xc} is the most challenging task in DFT procedures. For TDDFT, we find phenomena of interest when we approximate our Vxc for densities that change significantly over time. However, there are interesting phenomena where we do not need to vary the density in time that much. For example, we only need to apply a weak perturbation to the external potential V_{ext} at t to study low-lying excited states. We denote the density response to the perturbation δv_{ext} using Taylor expansion. This type of excited state has densities close to that of the initial state, so we only need up to the linear term. Writing $n(r,t) = n_{GS}(r) + \delta n(r,t)$. Therefore, the v_{xc} potential is now

$$v_{xc}[n_{GS} + \delta n](r,t) = v_{xc}[n_{GS}](r) + \int dt^{'} \int d^3r^{'} f_{xc}[n_{GS}](r, r^{'}, t - t^{'})\delta n(r^{'}, t^{'}), \qquad (2.44)$$

where the first term is the ground state v_{xc}, and the second term has the exchange-correlation kernel f_{xc}, which is the change of v_{xc} with respect to the linear response $\delta n(r,t)$. $\delta n(r,t)$ depends on a linear response function χ which tells you how the density changes with respect to the perturbation δv_{ext}. Following TDDFT formalism, there is a χ_{KS} for non-interacting KS electrons that yield the same density response $\delta n(r,t)$. If we equate the density response for interacting and non-interacting electrons and use the definition of f_{xc},

we obtain the TDDFT linear response equation (In frequency space)

$$\begin{aligned}\chi(r,r^{'},\omega) &= \chi_{KS}(r,r^{'},\omega) \\ &= \int d^3r_1 \int d^3r_2 \chi_{KS}(r,r_1^{'},\omega)\left\{\frac{1}{|r_1-r_2|}+f_{xc}(r_1,r_2,\omega)\right\}\chi(r_2,r^{'},\omega)\end{aligned} \tag{2.45}$$

where

$$\chi_{KS}(r,r^{'},\omega) = 2\lim_{\eta\to 0^+}\sum_q \left\{\frac{\xi_q(r)\xi_q^*(r^{'})}{\omega-\omega_q+i\eta}-\frac{\xi_q^*(r)\xi_q(r^{'})}{\omega+\omega_q-i\eta}\right\}. \tag{2.46}$$

The set of poles of eq.(2.45) are the excited state energies, and they appear when ω matches a true transition frequency, sending χ to infinity. There is a way of calculating the excited state energies by transforming eq.(2.45) into the Casida equations, where we have a matrix equation, the eigenvalues are the excited state energies, and the eigenvectors are the oscillator strengths.

2.2.5 Long Range Corrected (LRC) Functionals

Most functionals yield accurate transition energies for many complex organic systems. However, they describe poorly charge transfer energies in the molecule studied. To solve this problem, we employ Long Range Corrected (LRC) DFT Functionals. When the distance between electrons increases, these functionals use a growth parameter in the Hartree-Fock exchange. Dividing the Coulomb operator into long and short components,

$$\frac{1}{r} = \frac{1}{r}\left\{1-\left[\alpha+\beta erf\left(\gamma r\right)\right]\right\}+\frac{1}{r}\left[\alpha+\beta erf\left(\gamma r\right)\right], \tag{2.47}$$

where γ is the attenuation parameter, while α and β define the contributions of the Hartree-Fock exchange, in the case of the LRC functionals used in this study, LRC ωPBEh, we have 20% short-range HF exchange + 100% long range HF exchange + 80% ωPBE GGA exchange + PBE GGA correlation ($\omega = 0.2$) [38]. Thisω refers to the attenuation parameter γ, which needs tuning to our molecular system. This type of optimization is based on the Koopmans condition,

$$-\varepsilon_{HOMO}(N) = IE(N) \equiv E(N-1)-E(N). \tag{2.48}$$

The HOMO eigenvalue is equal to minus the ionization energy (IE), which is defined as the energy difference between the neutral and ionized molecule. Moreover, Baer and coworkers [39, 40, 41] suggest a tuning procedure that involves minimizing the sum of squares $(IE + \epsilon_{HOMO})^2$ for the neutral donor molecule and its analog for the anion of the acceptor species,

$$J(\gamma)^2 = |\epsilon_H^\gamma(N) + I_\gamma(N, \Delta SCF)|^2 + |\epsilon_H^\gamma(N+1) + I_\gamma(N+1, \Delta SCF)|^2 . \tag{2.49}$$

2.3 Perturbative DELTA-SCF

Another method to calculate excited state energies is the perturbative ΔSCF method developed in the NRLMOL code [42]. It is a simple DFT-based method for calculating the energy difference between the ground and the excited state. The difference between other ΔSCF methods is that it does not vary the density as in the self-consistency procedure to avoid the possible collapse of the excited state. Instead, an orthogonality condition is imposed between the ground and excited state wave functions. However, in practice, a perturbative approach relaxes the occupied orbitals,

$$\Delta H = \alpha \left(H_{ex} - H_g \right) \tag{2.50}$$

where α is a variational parameter to obtain the lowest excited state energy.

2.4 Computational Details

Most of the calculations with DFT presented in this thesis was carried out using the NRLMOL code originally developed by Mark Pederson [43, 44, 45, 46]. This code uses a Gaussian basis set that was optimized for the PBE functional [45]. Another salient feature of the code is that it is the first code to use a variational mesh for integration [43]. The mesh can be tuned for desired accuracy of the integrals. The perturbative delta-SCF method is implemented in this code [47, 48]. The TD-DFT calculations were performed using the Q-Chem code [49].

Chapter 3

Electronic structure of the Donor-Acceptor-Radical Supramolecule

The three component donor-acceptor-radical (D-A-R) supramolecular system that was employed to experimentally demonstrate teleportation of a spin state contains a 2,2,6,6-tetramethylbenzo[1,2- d:4,5-d]bis([1,3]dioxole), 4-aminonaphthalene-1,8-imide, and a α, γ-bisdiphenylene-β-phenylallyl which are shown in Fig. 3.1. These individual components were optimized first at the all-electron level using the PBE functional.

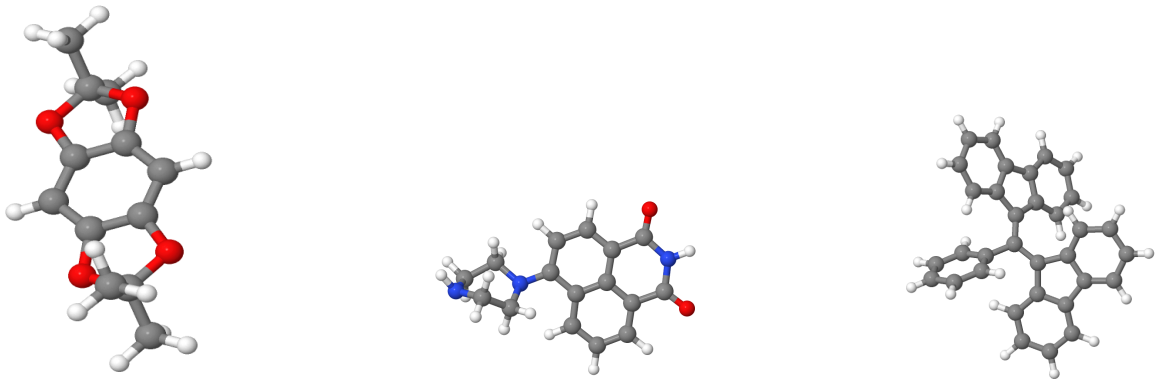

(a) Donor (b) Acceptor. (c) Radical

Figure 3.1: Optimized structure of individual component molecules of D-A-R complex system at PBE/NRLMOL level of theory

The initial structure of the supramolecule was constructed using these optimized components and the full molecule was further optimized. Since there is an unpaired electron located on the radical component, spin unrestricted calculations are carried out throughout.The

optimized structure of the full molecule is shown in Fig. 3.2.

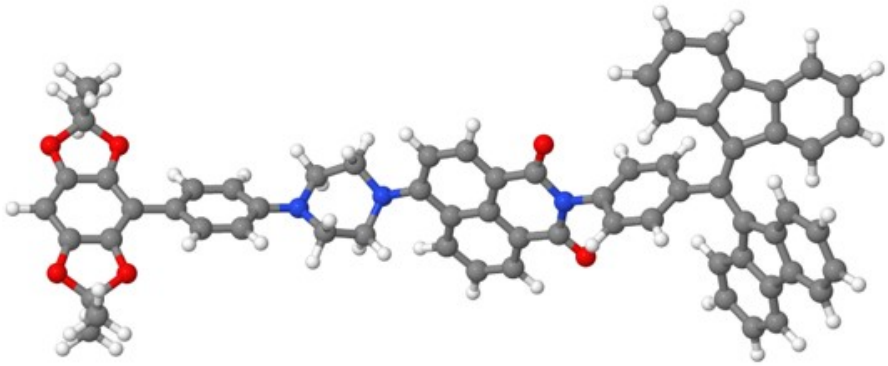

Figure 3.2: Optimized structure of complex D-A-R molecule at PBE/NRLMOL level of theory.

In the experiment reported in Ref. [11] the acceptor molecule is photoexcited to its first singlet excited state. The HOMO of the donor lies above the HOMO of the acceptor and as a result there is charge transfer from the donor HOMO to the acceptor HOMO leading to the formation of a $(D^+ - A^-)R$ charge transfer excited state. We point out that the experiments are carried out on the molecular sample solvated in toluene ($\epsilon = 2.38$).

The molecule in the ground state has a dipole moment of 3.10 Debye. The molecule has a length of ~ 21 Å and charge transfer states consequently have large dipole moments. The excited state dipole moments will interact with those of the solvent molecules surrounding it such that the dipole network will realign to minimize the energy of the system. The inclusion of solvent in the calculation of the excited states is therefore crucial. For consistency the ground state results shown below are calculated with toluene as solvent. The solvent is included using the polarizable continuum model (PCM).

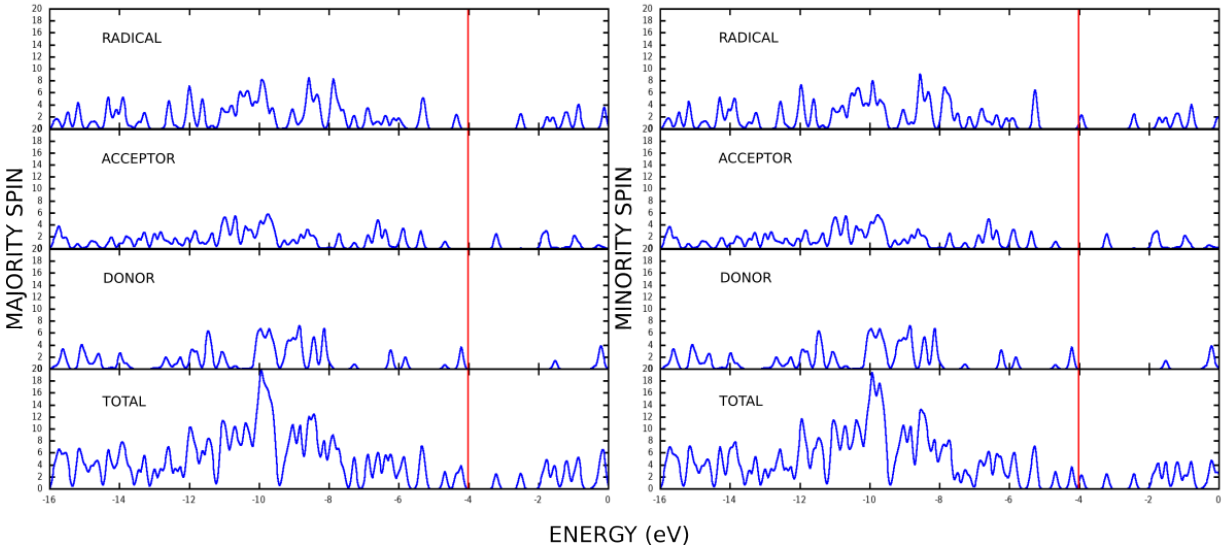

(a) Gas phase.

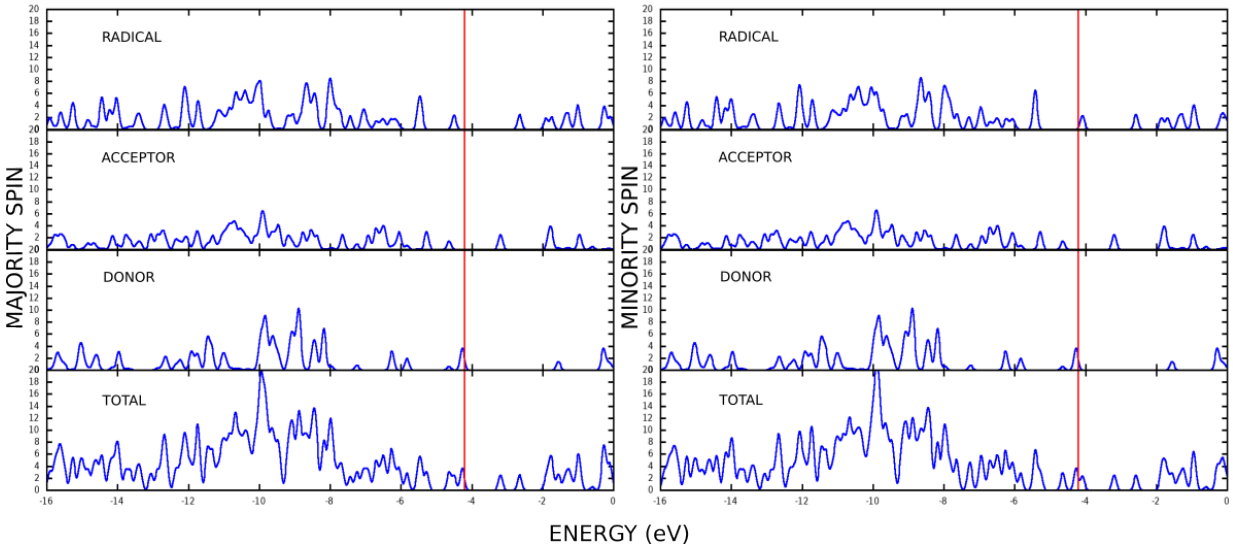

(b) Solution (toluene).

Figure 3.3: electronic density of States (DOS) in (a) gas phase and (b) in solution.

The site projected density of states of the molecule calculated with PBE functional are shown in Fig. 3.3 for both the gas phase and in solution of toluene. There is no significant difference between the DOS in gas phase and in solution except that the occupied orbitals are slightly stabilized in the solution. DOS clearly shows that the highest occupied

molecular orbital of the supramolecule is located on the donor component. The half-filled HOMO of the radical lies below the HOMO of the donor in the spin majority channel. The same orbital in the spin minority channel forms the LUMO of the molecule. Thus there is a large separation between the HOMO and the LUMO of the molecule which belong to opposite spin. The plots of the frontier orbital densities are shown in Fig. 3.4. In this plot, the red plots show the unoccupied orbitals and the blue color indicates an occupied orbital. Due to the unpaired electron on the radical there is a half-filled or singly occupied molecular orbital (SOMO) on the radical that lies below the donor HOMO. Likewise, there is an unoccupied (SUMO) on the radical which is the LUMO of the supramolecule. Thus the HOMO and LUMO of the supramolecule have opposite spins and spatially far apart. The next higher virtual orbital is located on the acceptor component. The DOS (Fig. 3.3) also roughly shows that the donor excitation energy is higher than that of the acceptor and the radical.

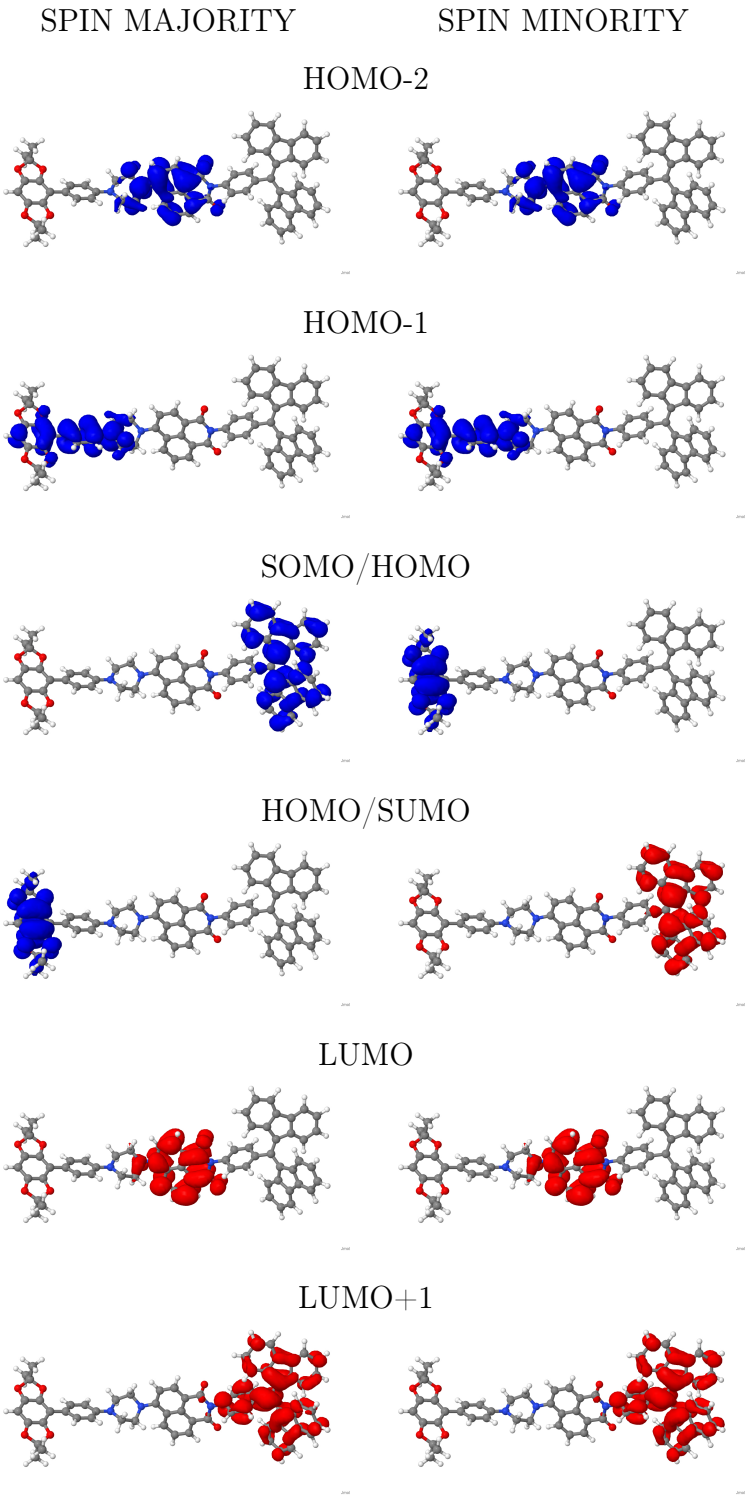

Figure 3.4: Highest occupied and lowest virtual molecular orbitals at IEF-PCM/PBE/6 31+G(d) level of theory (toluene $\varepsilon = 2.38$).

The DFT eigenvalue difference between the virtual and the occupied orbitals do not correctly show the excitation energies. The linear response time dependent DFT performs quite well in describing the absorption spectra particularly for the local excitations. The absorption spectra of the molecule calculated in solvated phase using PCM are shown in Fig. XX. These absorption spectra were calculated using TD-DFT linear response theory as implemented in the Q-Chem code. The calculated absorption spectra shows two prominent peaks between 330-600 nm with the hybrid functionals but with multiple peaks with the PBE functional. On the other hand LRC-wPBEh shows similar nature of the spectra as the other two hybrid functionals. For comparison, the experimental absorption spectra is reproduced in Fig. 3.6 from Ref. [11]. The UV-vis absorption spectra of the D-A-R and the same system but with a close shell version shows that the peak at 490 nm (2.53 eV) arises from the radical component only. The peak at 390 nm (3.20 eV) is due to absorption by the acceptor component. In the calculated spectra shown in Fig. 3.5, the first and second peaks (second and third peak for c)) of each graph correspond to the measured absorption maximum of the photoexcited acceptor $^{1\bullet}A$ and the radical $R^{\bullet}$, respectively. The calculated peak positions are also presented in Table 3.1 along with the experimental values. The hybrid functionals tend to open up the HOMO-LUMO gap with higher values for the peak positions. The values of the peak positions with different functionals are presented in Table 3.1.

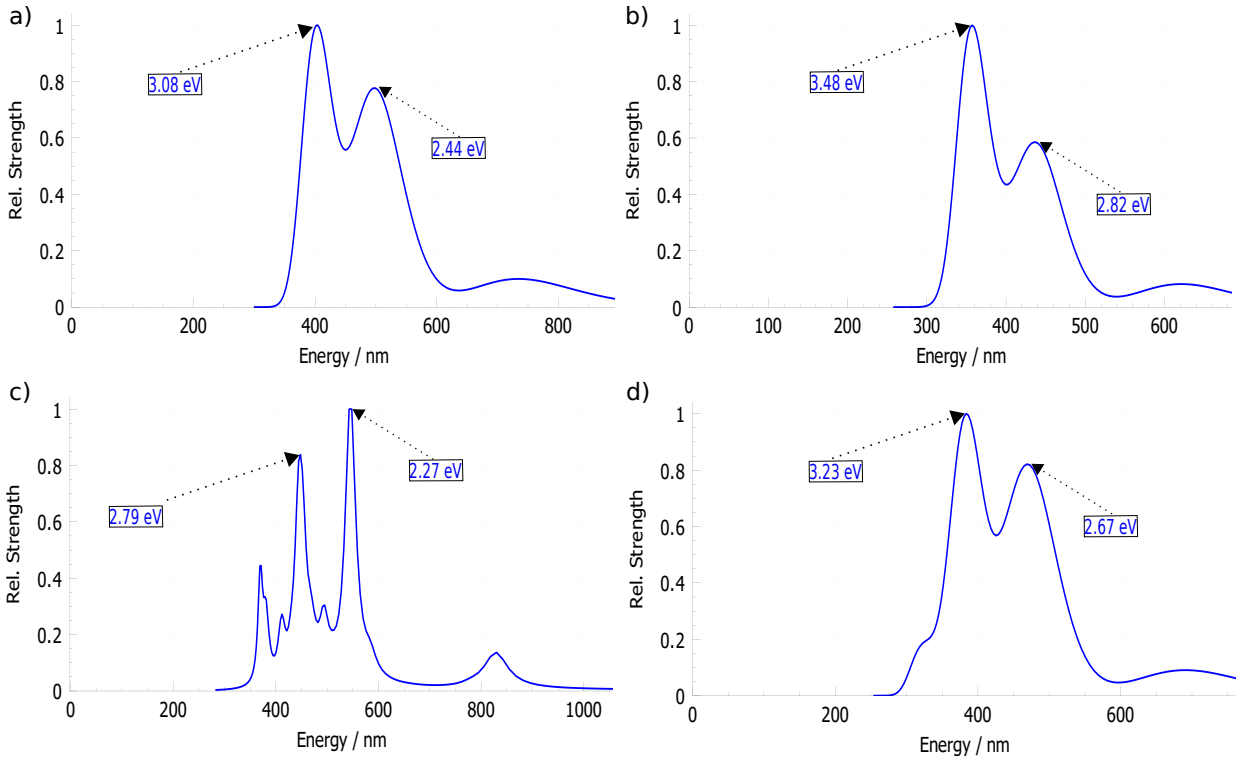

Figure 3.5: Calculated UV-vis absorption spectra of complex D-A-R at TDDFT/IEF-PCM/6-31+G(d) level of theory in toluene ($\varepsilon = 2.38$) solution with functional a) B3LYP b) CAM-B3LYP c) PBE d) LRC-ωPBEh with tuned attenuation parameter $\omega = 0.51$. The first and second peak (second and third peak for c)) of each graph correspond to the to the measured absorption maximum of the photoexcited acceptor $^{1*}A$ and radical $R^{\cdot}$, respectively.

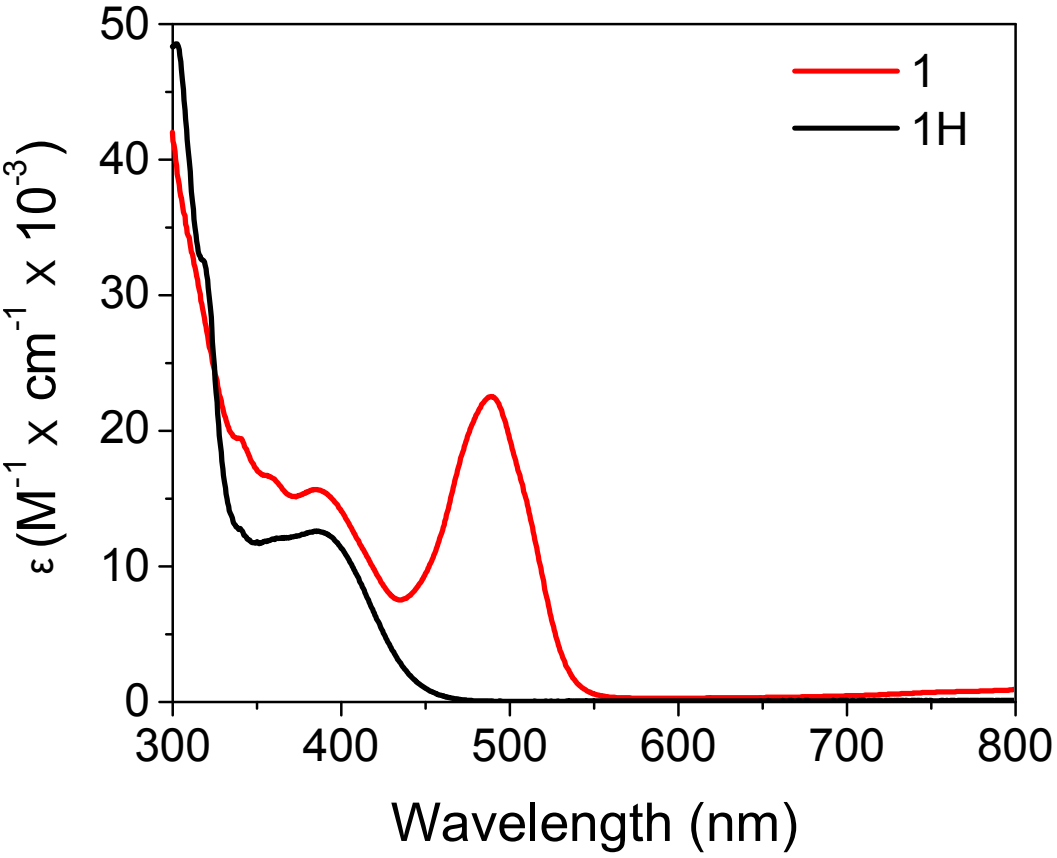

Figure 3.6: Experimental UV-vis absorption spectra of complex D-A-R in room temperature toluene ($\varepsilon = 2.38$) solution [11].

Table 3.1: TDDFT doublet vertical excitation energy corresponding to the measured absorption maximum of the photoexcited acceptor $^{1*}A$ and radical $R^{\bullet}$ for various DFT functionals.[α]

METHOD	$^{1*}A$			$R^{\cdot}$		
	eV	nm	DIFF.	eV	nm	DIFF.
B3LYP	3.08	403	0.12	2.44	508	0.09
CAM-B3LYP	3.48	340	0.28	2.82	428	0.29
PBE[β]	2.79	444	0.41	2.27	546	0.26
LRC-ωPBEh[γ]	3.23	384	0.03	2.67	464	0.14
expt.	3.20	388		2.53	490	

[α]Calculations were done using 6-311+G(d) basis set, and IEF-PCM solvation model in toluene ($\epsilon = 2.38$).

[β]Same results for perturbative ΔSCF NRLMOL.

[γ]Tuned attenuation parameter ($\omega = 0.51$).

The excited states that are relevant for the quantum processes are the charge transfer excited states. Two such states in which the hole is located on the donor and particle is located on the acceptor or radical are pictorially shown in Figs. 3.7. As shown these states have very large particle and hole separation and as a result large dipole moments. The effect of the solvents is strong in stabilizing such states.

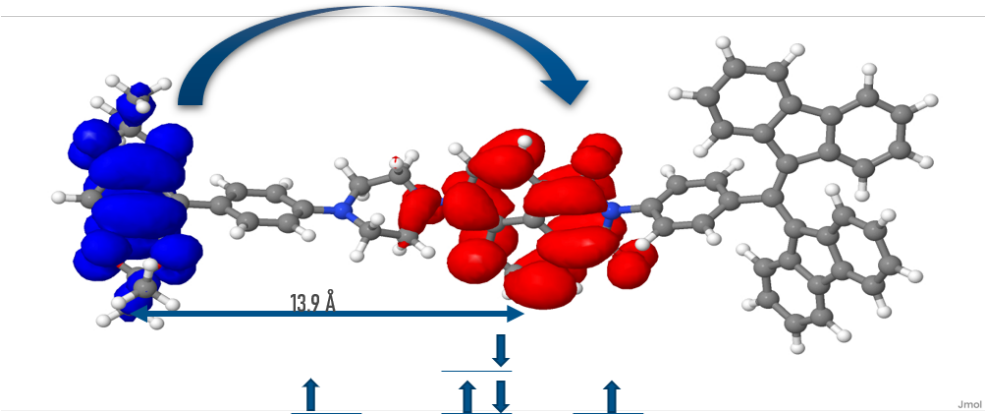

Figure 3.7: Orbitals participating in the donor (Blue) to acceptor (Red) electron transition to form charge-separated state $D^+A^-R^{\cdot}$ with center-to-center distance of 13.9 Å.

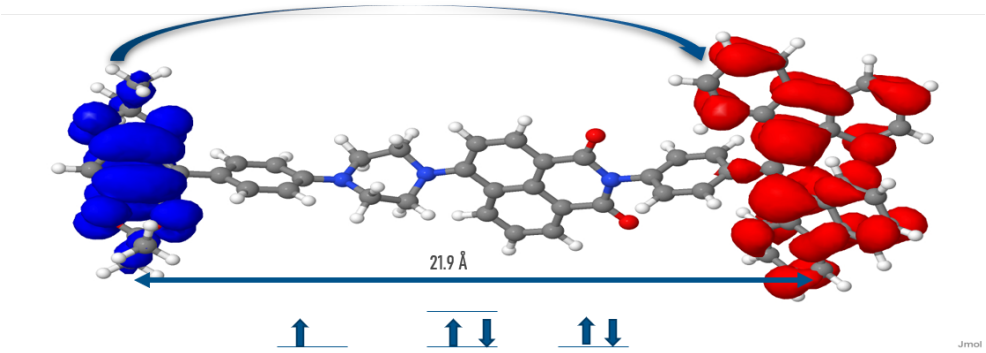

Figure 3.8: Orbitals participating in the donor (Blue) to radical (Red) electron transition to form charge-separated state D^+AR^- with center-to-center distance of 21.9 Å.

An estimate of the charge transfer excited states can be made from Mulliken equation which gives the excited state energy as $E_{ex} = IP - EA - \frac{1}{R}$ where, IP is the ionization potential of the component with the hole, EA is the electron affinity of the component where the electron moves to, and R is the separation between them. The calculated ionization potential (IP) of the isolated donor in gas phase is 6.50 eV. Similarly, the electron affinities (EA) of the isolated acceptor molecule and the radical in gas phase are is 1.13 and 2.50 eV, respectively. Considering a separation of 13.9 between the particle and the hole, an

estimate of the excited state from Mulliken equation is 4.23 eV. In the presence of toluene, the ionization potential reduces to 5.56 eV whereas the EA values increase to 2.11 and 3.36 eV for the acceptor and the radical, respectively. The energy of this charge transfer state then reduces to 3.02 eV. This energy estimate does not include the relaxation of the passive orbitals.

The charge transfer excited states are calculated with the NRLMOL code using the perturbative delta-SCF method. These calculations are carried out using the PBE functional. We also used the range corrected LRC-ωPBEh functional in the TD-DFT formalism to calculate the energies of the relevant excited states. These excitation energies are listed in Table 3.2. The agreement between the perturbative delta-SCF emthod and TD-DFT is excellent for the $D^+A^- - R$ state, but it is on the order on 0.1 eV for the $(D^+ - A - R^-)$ state. The experimental estimates for these energies are made from the data using CH2Cl2 as solvent which was used in Weller equation to derive the estimates in toluene. The differences between the calculated excitation energy and experimental energies are, however, large. these differences lie between 0.3 - 0.6 eV for the two charge transfer states. We point out that ionic relaxation of the molecule is not taken into account in the calculations which may explain the differences. We also emphasize that the perturbative delta-SCF method works well for charge transfer excitations, but does not predict the local excitation with similar accuracy. Overall, we see the same trend - that the $D^+ - A^- - R$ state is higher in energy compared to the $D^+ - A - R^-$ state.

Table 3.2: Charge transfer energies (CTE) of the charge-separated states in the DAR complex calculated with different excited state methods.[α]

Method	D → A (eV)	DIFF.	D → R (eV)	DIFF.
	$D^+A^-R^{\cdot}$		D^+AR^-	
[β]NRLMOL (PBE)	2.82	0.30	2.03	0.69
TDDFT (LRC-ωPBEh)	2.81	0.29	2.16	0.82
IP^D-$EA^{A/R}$-$\frac{1}{r}$ (PBE)	3.02	0.52	1.93	0.59
Ref. (Weller equation)	2.52		1.34	

[α]Calculations in toluene ($\epsilon = 2.38$) solution with IEF-PCM.

[β]Perturbative ΔSCF Excited state method

3.1 Spin Hamiltonian

The charge transfer excited states constitute three-spin states. The spins on the components for the two charge states shown in Fig. 3.7 and 3.8. Since the entanglement of the spins on the D, A, R sites are of interest, we further calculated the magnetic exchange parameters J between the donor and the acceptor, and acceptor and the radical sites. To do that, energies of three spin states are calculated using the perturbative delta-SCF method. These spin configurations are schematically shown in Fig. 3.9a and their respective energies are shown in Fig. 3.9b. The J parameters are calculated using the following definitions for the spin states 1, 2, and 3:

$$E_1 = E_0 + J_{23} S_D.S_A + J_{12} S_A.S_R$$

$$E_2 = E_0 + J_{23} S_D.S_A - J_{12} S_A.S_R$$

$$E_3 = E_0 - J_{23} S_D.S_A + J_{12} S_A.S_R$$

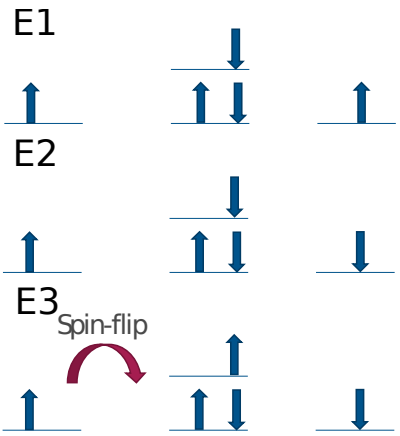

(a)

	eV
E1	2.81935
E2	2.81881
E3	2.81919

(b)

	meV	cm^{-1}
J_{DA}	0.00033	2.63364
J_{AR}	0.00109	8.77881

(c)

Figure 3.9: a) Spin configurations corresponding to the b) Heisenberg Hamiltonian energies needed to calculate c) Magnetic-Exchange coupling constants of the donor-acceptor (J_{DA}) and acceptor-radical (J_{AR}) electron spin pairs.

The exchange parameters indicate higher exchange interaction between the acceptor and the radical compared to that between donor and acceptor. The center to center diance between the donot and acceptor is twice larger compared to that between the acceptor and the radical, which is reflected in the difference between the two J parameters.

The time evolution of such systems are generally modeled using the magnetic Hamiltonian which is expressed in spin basis. In such models the spatial part of the wavefunction is integrated out. In this work we develop a model where both spatial and spin part will be taken into account. The parameters calculated with DFT is utilized to develop the model Hamiltonian. This model is described in the next chapter.

Chapter 4

Simple Model Hamiltonian

The spin state teleportation process includes the following steps: a) photoexcitation of the acceptor b) electron transfer from the donor to the acceptor or hole transfer from acceptor to the donor c) electron transfer from the acceptor to the radical. A simulation of the dynamics requires at least N=10 orbitals that are most relevant for the process. These are the donor HOMO, donor LUMO, acceptor HOMO, acceptor LUMO, radical HOMO, and radical LUMO. Considering that both spins are relevant here, the total number of spin orbitals is N=10. To simplify this work, we consider only one spin in the radical center for each orbital, reducing the total number of spin orbitals to N=6. The radical HOMO and LUMO have same space extent as can be seen from the orbital density. The motivation for this Hamiltonian is to reduce the N-electron Hamiltonian to a 3-electron Hamiltonian. The electronic orbitals will depend both on space and spin. These orbitals will be expressed in the basis of the above mentioned orbitals in a simplified form. We assume that each of the orbitals are centered either on the donor, acceptor, or on the radical. We express the orbitals as linear combination of Gaussian centered on these locations. These locations are determined from the centroids of the actual molecular orbitals and are called C_i in the discussion below.

We write the Hamiltonian model as follows,

$$\begin{aligned}\hat{H}_{model} &= -\sum_{i}^{N} \frac{\nabla_i^2}{2m_i} - \sum_{i}^{N} V_i e^{-\beta_i (r-C_i)^2} \\ &= T_{model} + V_{model}. \end{aligned} \tag{4.1}$$

The first term is the kinetic energy with a mass m_i for each of the N=6 states. In contrast, the second term describes the system's potential energy using a simplified screened coulomb

potential centered at C_i with constant potential V_i representing the strength of interaction at long distances and screening length β_i. This parameter characterizes how quickly the screening effect decays with distance. In this case, we have an occupied and unoccupied state at each center, meaning that C_i is the same in every two states. Now that we have our Hamiltonian model, we also need to model the molecular orbitals representing the quantum states of our molecule, i.e., construct a basis set. In this case, we use Cartesian Gaussian-type orbitals (GTO) expressed as follows in radial-angular decomposition,

$$\Psi_i^{model} = \sum_{n_x n_y n_z}^{N} \psi_{n_x n_y n_z} P_{n_x n_y n_z} e^{-\alpha_i (r - C_i)^2}, \tag{4.2}$$

where,

$$P^i_{n_x n_y n_z} = (x - C_{ix})^{n_x} (y - C_{iy})^{n_y} (z - C_{iz})^{n_z}. \tag{4.3}$$

We use a single bare Gaussian centered at C_i with width parameter α_i for the radial part and homogeneous polynomials $P^i_{n_x n_y n_z}$ in Cartesian coordinates centered atC_i for the angular part, these polynomials are categorized by their angular momentum quantum number $L = n_x + n_y + n_z$. In essence, we have an orbital defined by a linear combination of homogeneous polynomials depending on L with coefficients $\psi_{n_x n_y n_z}$ characterized by a single Gaussian.

Having defined the model Hamiltonian and orbitals, it is time to fit them into the molecular system employed in the previous chapter. Thus, we will examine the multipole moments, the kinetic and potential energy of the orbitals of interest from the simulations using the NRLMOL code. First, we are interested in the highest occupied molecular orbitals (HOMO) and lowest unoccupied molecular orbitals (LUMO) of the donor, acceptor and radical components of the complex molecule where all the interesting properties appear, as mentioned in the previous chapter. Then, we obtain the multipole moments in Cartesian coordinates of each orbital as shown in the first half of Table 4.1, where we will use the centroids ($\langle x \rangle$ $\langle y \rangle$ $\langle z \rangle$) as the three centers of our model; HOMO and LUMO of the donor at one center, and the same for the acceptor and radical orbitals. Hence, The second half of Table 4.1 shows the centered moments used as data for the fitting procedure. In a similar

manner, we also need the kinetic and potential energy of these oribtals, where the potential energy is the difference between the kinetic and total energy as shown in Table 4.2.

Table 4.1: DAR molecule multipole moments $(a_0)^n$ for optimization process.

Moments	**C1:Donor**		**C2:Acceptor**		**C3:Radical**	
	HOMO	**LUMO**	**HOMO**	**LUMO**	**HOMO**	**LUMO**
$\langle x \rangle$	24.16	19.94	2.75	-0.60	-18.07	-16.08
$\langle y \rangle$	1.43	0.40	-1.76	-3.27	1.22	0.89
$\langle z \rangle$	-2.25	-1.03	2.93	2.56	-0.61	-0.14
$\langle x^2 \rangle$	587.11	432.92	28.63	16.04	336.49	277.07
$\langle y^2 \rangle$	6.95	4.44	10.48	23.52	26.23	16.75
$\langle z^2 \rangle$	17.74	7.80	11.03	8.98	9.08	7.25
$\langle xy \rangle$	35.82	14.36	-5.62	2.61	-20.03	-16.03
$\langle xz \rangle$	-52.77	-28.03	8.96	0.304	13.35	5.55
$\langle yz \rangle$	2.23	-1.65	-4.88	-7.65	7.19	4.19
CENTERED MOMENTS						
$\langle x - \langle x \rangle \rangle \, \mu_{100}$	0	0	0	0	0	0
$\langle y - \langle y \rangle \rangle \, \mu_{010}$	0	0	0	0	0	0
$\langle z - \langle z \rangle \rangle \, \mu_{001}$	0	0	0	0	0	0
$\langle x - \langle x \rangle \rangle^2 \, \mu_{200}$	3.42	35.32	21.05	15.68	9.82	18.5
$\langle y - \langle y \rangle \rangle^2 \, \mu_{020}$	4.91	4.28	7.39	12.83	24.75	15.96
$\langle z - \langle z \rangle \rangle^2 \, \mu_{002}$	12.70	6.74	2.45	2.43	8.71	7.23
$\langle (x - \langle x \rangle)(y - \langle y \rangle) \rangle \, \mu_{110}$	1.28	6.38	-0.77	0.65	1.94	-1.72
$\langle (x - \langle x \rangle)(z - \langle z \rangle) \rangle \, \mu_{101}$	1.51	-7.49	0.89	1.84	2.31	3.30
$\langle (y - \langle y \rangle)(z - \langle z \rangle) \rangle \, \mu_{011}$	5.44	-1.24	0.27	0.72	7.93	4.32

Table 4.2: DAR molecule Kinetic and Total Energy for optimization process.

Center	Kinetic Energy (Ha)		Total Energy (Ha)	
	HOMO	LUMO	HOMO	LUMO
Donor	2.09	1.70	-0.16	-0.06
Acceptor	1.61	1.77	-0.19	-0.12
Radical	1.39	1.55	-0.17	-0.15

Before calculating the expected value of the multipole moments, we need to determine whether the orbitals are s (L=0), p (L=1), d (L=2), or of higher angular momentum by looking at the density of states (DOS) of each center and inspecting the highest L contributions of the corresponding HOMO and LUMO as shown in fig 4.1. In that matter, center 1 HOMO is a combination of type-d (L=2), type-g (L=4) and type-I (L=6) orbital and LUMO is a combination of type-f (L=3) and type-h (L=5) orbital; center 2 HOMO is a combination of type-f (L=3) and type-h (L=5) orbital and LUMO is a combination of type-p (L=1) and type-f (L=3) orbital; center 3 HOMO is a combination of type-d (L=2), type-f (L=3) and type-g (L=4) orbital and LUMO is a combination of type-f (L=3), type-h (L=5) and type-d (L=2) orbital.

We decided to use GTOs for various reasons: Gaussian functions have mathematical properties that allow analytically evaluating many integrals. This feature simplifies the computation of the molecular moments, the kinetic and potential energy. GTOs also maintain their mathematical properties when combined and transformed, ensuring that their linear combinations remain Gaussian-type functions, simplifying more calculations of molecular properties. Moreover, their adjustable width α allows them to be concentrated near the nucleus, making it suitable for calculations the more localized the state is. Putting these properties to work, we devised mathematical recipes for the multipole moments, the kinetic and potential energy in equations (4.4), (A.3), and (A.1), respectively. These expectation values are defined by the model Hamiltonian measured on model orbitals

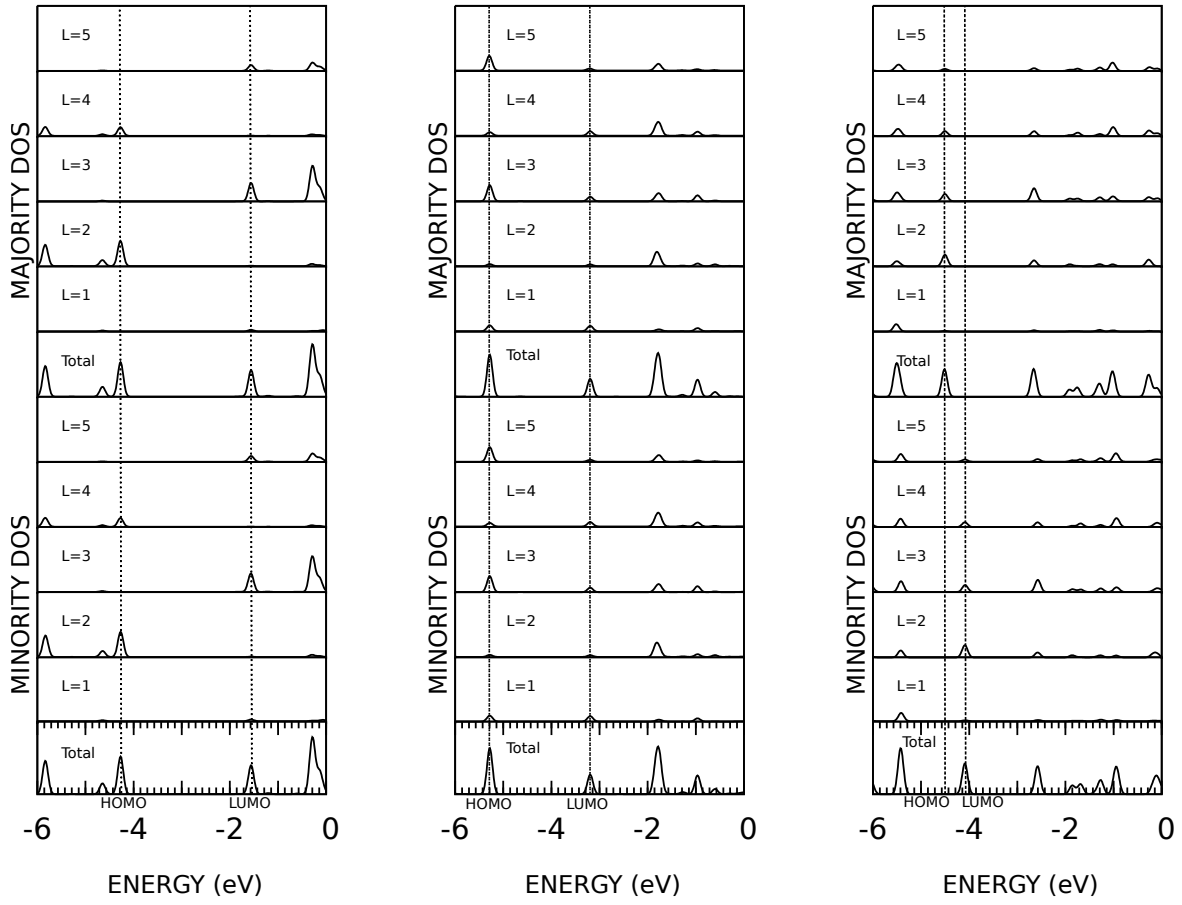

(a) C1:Donor HOMO -4.35 eV and LUMO -1.63 eV.

(b) C2:Acceptor HOMO -5.17 eV and LUMO -3.27 eV.

(c) C3:Radical HOMO -4.63 eV and LUMO -4.08 eV.

Figure 4.1: Pictured above are the electronic density of states (DOS) corresponding to the three centers selected for the model Hamiltonian. For each spin, the total DOS and angular momentum contributions from $L = 1$ to $L = 5$ are presented. The two vertical dotted lines represent the energy of the highest occupied and lowest unoccupied molecular orbitals (HOMO's and LUMO's) for each spin. Units are arbitrary, but the same scale has been used for all DOS plots.

mentioned at the start of the chapter. It is also important to mention the calculation of the overlap integral between the same state in equation (A.2), as it will serve as the normalization constant of each observable computed. The multipole moments have the following expression,

$$\begin{aligned}
\left\langle \Psi_i^{model} \left| P_{mjk}^i \right| \Psi_i^{model} \right\rangle &= \int d^3r \Psi_i^{*model} (x - C_{ix})^m (y - C_{iy})^j (z - C_{iz})^k \Psi_i^{model} \\
&= \sum_{n_x n_y n_z}^{N} \sum_{p_x p_y p_z}^{N} \psi_{n_x n_y n_z} \psi_{p_x p_y p_z} \{ \int dx e^{-2\alpha x^2} x^{m+\mathrm{nx}+\mathrm{px}} \\
&\times \int dy e^{-2\alpha y^2} y^{j+\mathrm{ny}+\mathrm{py}} \int dz e^{-2\alpha z^2} z^{k+\mathrm{nz}+\mathrm{pz}} \} \\
&= \sum_{n_x n_y n_z}^{N} \sum_{p_x p_y p_z}^{N} \psi_{n_x n_y n_z} \psi_{p_x p_y p_z} \{ \left((-1)^{j+\mathrm{ny}+\mathrm{py}} + 1 \right) \left((-1)^{k+\mathrm{nz}+\mathrm{pz}} + 1 \right) \\
&\times \left((-1)^{m+\mathrm{nx}+\mathrm{px}} + 1 \right) \Gamma \left(\frac{1}{2} (j + \mathrm{ny} + \mathrm{py} + 1) \right) \\
&\times \Gamma \left(\frac{1}{2} (k + \mathrm{nz} + \mathrm{pz} + 1) \right) \Gamma \left(\frac{1}{2} (m + \mathrm{nx} + \mathrm{px} + 1) \right) \\
&\times 2^{\frac{1}{2}(-j-\mathrm{ny}-\mathrm{py}-3)+\frac{1}{2}(-k-\mathrm{nz}-\mathrm{pz}-3)+\frac{1}{2}(-m-\mathrm{nx}-\mathrm{px}-3)} \\
&\times \alpha^{\frac{1}{2}(-j-\mathrm{ny}-\mathrm{py}-1)+\frac{1}{2}(-k-\mathrm{nz}-\mathrm{pz}-1)+\frac{1}{2}(-m-\mathrm{nx}-\mathrm{px}-1)} \}
\end{aligned} \tag{4.4}$$

where the type of moment depends on $L = m + j + k$, which we differentiate the orbital model polynomials with $L = n_x + n_y + n_z$ and $L = p_x + p_y + p_z$to include the double sum over $N = (L + 1)(L + 2)/2$ polynomials. To compute the integral, we changed to a Cartesian coordinates system, neglected the center for integrals between the same state, and left with three integrals that we can compute using tables of integrals. Then, the final result for the multipole moment is a double sum over the left state with coefficients $\psi_{n_x n_y n_z}$ and right side with coefficients $\psi_{p_x p_y p_z}$, a product of a condition that takes integral to zero for L odd, Gamma function, and constant values 2α that come from the arguments of the Gaussian with additional products corresponding to each Cartesian coordinate. We have a similar expression for the normalization constant kinetic and potential energy, but without the moment indices m,j,k. in particular, the potential energy has an additional β value in the evaluation of the Gaussian, and the kinetic energy has an additional expression that

breaks up the result into three parts due to the evaluation of the Laplacian ∇^2. We can see the similarities with the equations expressed in AppendixA.

The performance of the model depends on the input values (parameters) given to the orbital coefficients $\psi_{n_x n_y n_z}$, Gaussian width α, potential parameters V and β, and the mass m coming from the kinetic energy. Therefore, we need an objective function to quantify the discrepancy between the model's predictions and the target values,

$$\begin{aligned}\chi_i^2 = &(\frac{\langle P^i_{200}\rangle}{\langle \Psi_i^{model} \mid \Psi_i^{model}\rangle} - \mu^i_{200})^2 + (\frac{\langle P^i_{110}\rangle}{\langle \Psi_i^{model} \mid \Psi_i^{model}\rangle} - \mu^i_{110})^2 \\ &+ (\frac{\langle P^i_{020}\rangle}{\langle \Psi_i^{model} \mid \Psi_i^{model}\rangle} - \mu^i_{020})^2 + (\frac{\langle P^i_{101}\rangle}{\langle \Psi_i^{model} \mid \Psi_i^{model}\rangle} - \mu^i_{101})^2 \\ &+ (\frac{\langle P^i_{011}\rangle}{\langle \Psi_i^{model} \mid \Psi_i^{model}\rangle} - \mu^i_{011})^2 + (\frac{\langle P^i_{002}\rangle}{\langle \Psi_i^{model} \mid \Psi_i^{model}\rangle} - \mu^i_{002})^2 \\ &+ (\frac{\langle T^i_{model}\rangle}{\langle \Psi_i^{model} \mid \Psi_i^{model}\rangle} - KE_i)^2 + (\frac{\langle V^i_{model}\rangle}{\langle \Psi_i^{model} \mid \Psi_i^{model}\rangle} - PE_i)^2 \end{aligned} \tag{4.5}$$

that we defined as a sum of squares of the difference between the normalized computed integrals and the observed values in the NRLMOL code of the ith orbital, which are the six moments from L=2, and the kinetic and potential energy. Consequently, we find the model parameters that optimize the objective function (minimize or maximize) to obtain the best results. Our objective function is nonlinear and has many parameters, so we started the optimization process using the conjugate-gradient and Newton's method, but the resulting parameters fall outside the region of interest to the extent of obtaining complex values. Then, we had to add constraints to some parameters and resort to Mathematica's numerical algorithm for nonlinear constrained local optimization, the Interior Point Algorithm. This algorithm adds a barrier function defined by the Karush-Kuhn-Tucker (KKT) conditions to the objective function to include an inequality constraint, resulting in a nonlinear system that we can solve using Newton's method. It is called the interior point method, as it only searches for points in the interior of the feasible region. However, there are still too many parameters to handle, resulting in values that do not perform well with the model. For this reason, we designed an optimization scheme based on fixing parameters. The first optimization step requires fixing all parameters but the orbital coefficients $\psi_{n_x n_y n_z}$

and sets all initial values to one. The second step only varies the Gaussian width α, sets the optimized $\psi_{n_x n_y n_z}$ from the step before as initial values (the other ones are one), and constraints $\alpha \geq 0$. The third step varies the potential parameters β and V, sets the optimized $\psi_{n_x n_y n_z}$ and α from previous steps as initial values (the other ones are one), and constraints β, $V \geq 0$. The last step only varies the mass, sets the previous optimized $\psi_{n_x n_y n_z}$, α, β and V as initial values, and constraints $V \geq 0$. Finally, we repeat this process a certain amount of times depending on the objective function. All optimization steps are shown with red, green, cyan, and magenta dots in the optimization path plots for each orbital in Figure 4.2.

Before examining the optimized model's accuracy, mentioning the treatment applied to the dataset is essential. In this case, we applied a root transformation to each data point in the dataset. This transformation can reduce the sensitivity of the data to changes in the parameters, which appears considerably in our objective function due to the high interaction between parameters. By transforming the data, the impact of small changes in the parameters is dampened, providing a more stable and predictable optimization process, which in return leads to faster and more reliable convergence. Then, we applied the optimization process mentioned before for root values between 2-6 in increments of 0.1 to find the optimal root (smallest minimum for the objective function) in each model orbital, as shown in Figure 4.3. The optimal root for center 1 HOMO/LUMO are 1 and 1.3, center 2 HOMO/LUMO are 1.9 and 1.5, and center 3 HOMO/LUMO are 1.3 and 1.3.

To demonstrate the accuracy of the model, we calculated the six multipole, kinetic and potential energy with the parameters obtained using the optimization process described above. All parameters are reported with two decimals of precision in Appendix B. Figure 4.4 summarizes the accuracy of the model characterized by the percent error between the observable calculated with the model and the one calculated in NRLMOL. All the errors are below 0.1%, indicating a good model performance.

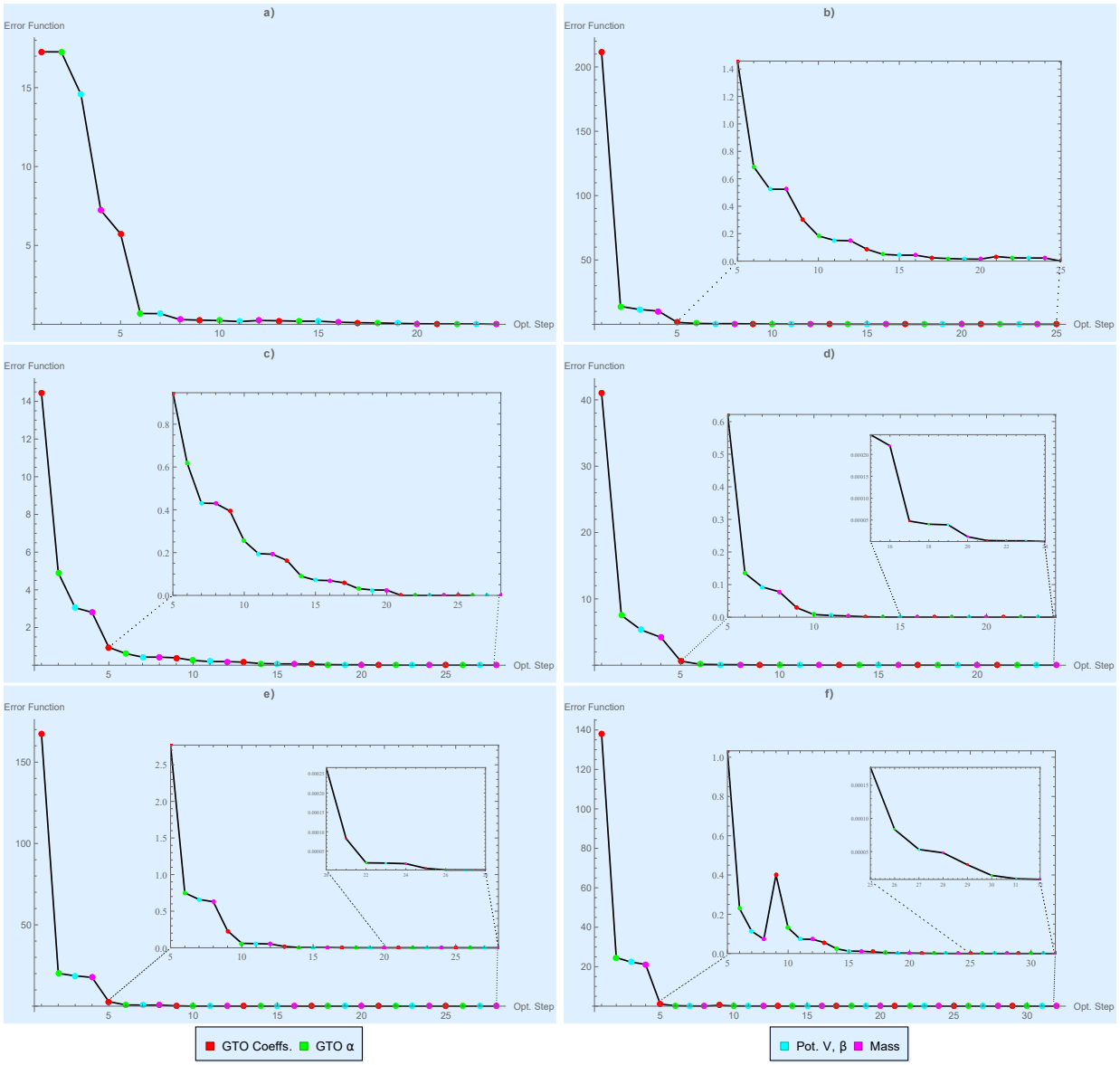

Figure 4.2: Optimization path corresponding to fitted a) center 1 HOMO and b) LUMO, c) center 2 HOMO and d) LUMO, and e) center 3 HOMO and f) LUMO. The red dots correspond to optimization varying wavefunction coefficients; green dots correspond to optimization varying the Gaussian width α; cyan dots correspond to optimization varying the potential parameters β and V; and magenta dots correspond to optimization varying the mass of the system.

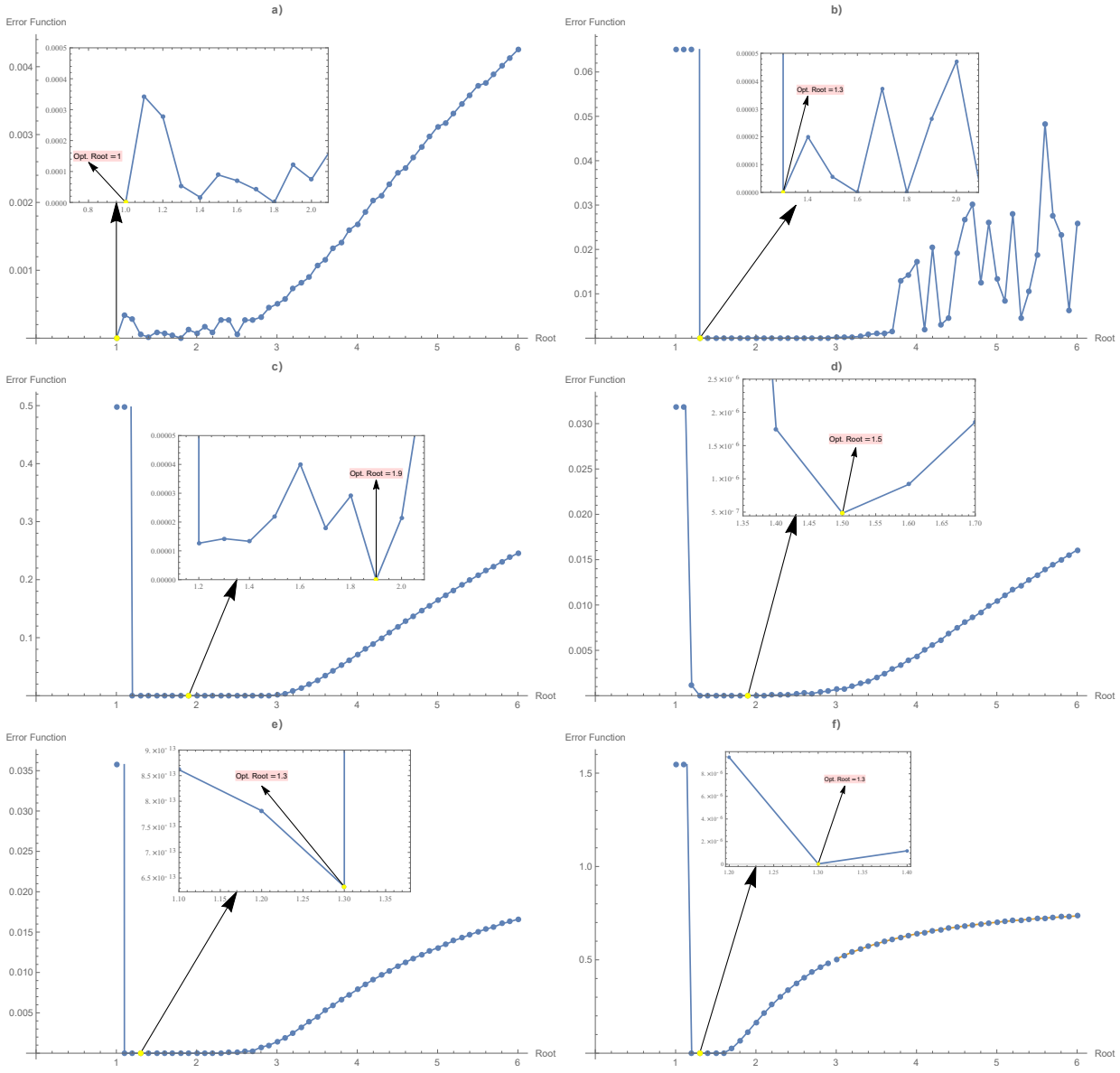

Figure 4.3: Plots showing the search (between 1 and 6 in steps of 0.1) of optimal value for root transformation of original data corresponding to fitted a) center 1 HOMO and b) LUMO, c) center 2 HOMO and d) LUMO, and e) center 3 HOMO and f) LUMO. Zooming in to the smallest error function, one can identify the optimal root value as shown in the smaller plots.

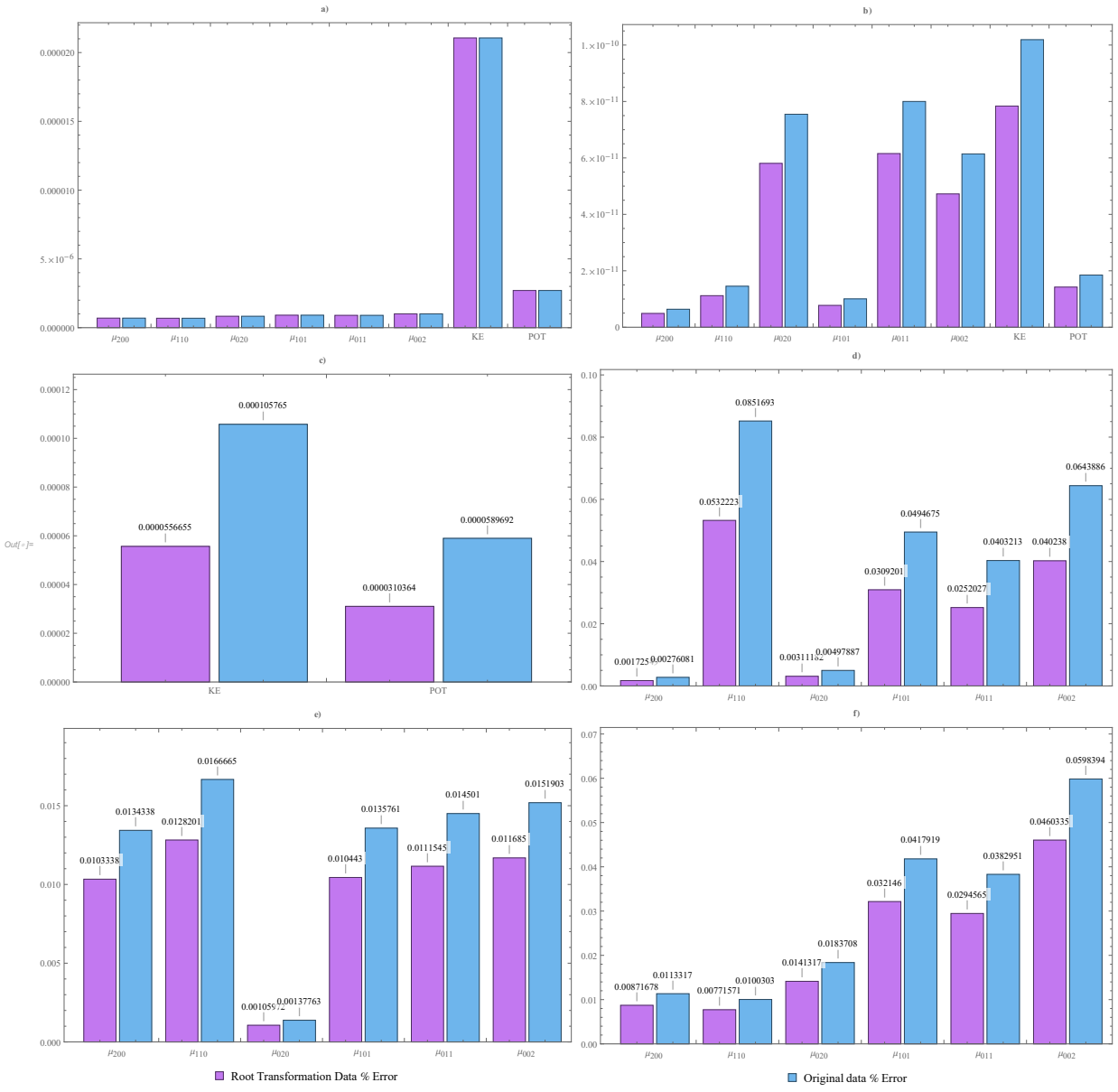

Figure 4.4: Bar charts of Percent errors between original (root) data set and values corresponding to fitted a) center 1 HOMO and b) LUMO, c) center 2 HOMO and d) LUMO, and e) center 3 HOMO and f) LUMO. Some observables are missing since their error is small compared to others.

Chapter 5

Conclusions

We have presented a DFT analysis of the ground state and excited state properties of the complex molecule employed for experimental quantum teleportation. In summary, solvent polarity plays an essential role in ordering the orbitals; Charge transfer energies change with solvent polarity, but we find that due to the ionic nature of the complex system, even low polarity solvents make a significant change in energies. Moreover, local excitations energies improve with the tuning of LRC-ωPBEh in TDDFT. Otherwise, energies are similar to perturbative ΔSCF. Regarding the computational methods, perturbative ΔSCF is as accurate as TDDFT with tuned LRC-ωPBEh for charge transfer energies. However, perturbative ΔSCF allows more straightforward spin-flip excited state calculations. Regarding the Simple Hamiltonian Model, we designed an orbital optimization scheme that predicts the multipole moments, the kinetic and potential energy of the complex molecular orbitals within a percent error of 0.1%.

5.1 Future Work

In future the model Hamiltonian will be employed to study the dynamical properties o the system using a procedure similar to electron dynamics. This model captures the essence of the electronic orbitals while reducing the complexities of the large molecule. The next steps will be to use these orbitals as the basis function to determine the orbitals for the 3-electron systems. This will allow us to determine the transition times. This step however still requires using an integration mesh for numerical integrations. In future we will use the parameters derived from the DFT calculations to determine more properties, such as

transition probabilities or the effect of external stimuli (electric or magnetic field).

References

[1] A. Cesa and J. Martin. Two-qubit entangling gates between distant atomic qubits in a lattice. *Phys. Rev. A*, 95:052330, May 2017.

[2] Daniel Loss and David P. DiVincenzo. Quantum computation with quantum dots. *Phys. Rev. A*, 57:120–126, Jan 1998.

[3] Jens Koch, Terri M. Yu, Jay Gambetta, A. A. Houck, D. I. Schuster, J. Majer, Alexandre Blais, M. H. Devoret, S. M. Girvin, and R. J. Schoelkopf. Charge-insensitive qubit design derived from the cooper pair box. *Phys. Rev. A*, 76:042319, Oct 2007.

[4] Marcus W. Doherty, Neil B. Manson, Paul Delaney, Fedor Jelezko, JÃ¶rg Wrachtrup, and Lloyd C.L. Hollenberg. The nitrogen-vacancy colour centre in diamond. *Physics Reports*, 528(1):1–45, 2013. The nitrogen-vacancy colour centre in diamond.

[5] C. Ospelkaus, U. Warring, Y. Colombe, K. R. Brown, J. M. Amini, D. Leibfried, and D. J. Wineland. Microwave quantum logic gates for trapped ions. *Nature*, 476(7359):181–184, Aug 2011.

[6] V. M. Schäfer, C. J. Ballance, K. Thirumalai, L. J. Stephenson, T. G. Ballance, A. M. Steane, and D. M. Lucas. Fast quantum logic gates with trapped-ion qubits. *Nature*, 555(7694):75–78, Mar 2018.

[7] Michael N. Leuenberger and Daniel Loss. Quantum computing in molecular magnets. *Nature*, 410(6830):789–793, Apr 2001.

[8] Daniel Loss and David P. DiVincenzo. Quantum computation with quantum dots. *Phys. Rev. A*, 57:120–126, Jan 1998.

[9] M. H. Devoret and R. J. Schoelkopf. Superconducting circuits for quantum information: An outlook. *Science*, 339(6124):1169–1174, 2013.

[10] P. J. Hore, Konstantin L. Ivanov, and Michael R. Wasielewski. Spin chemistry. *The Journal of Chemical Physics*, 152(12):120401, 2020.

[11] Brandon K. Rugg, Matthew D. Krzyaniak, Brian T. Phelan, Mark A. Ratner, Ryan M. Young, and Michael R. Wasielewski. Photodriven quantum teleportation of an electron spin state in a covalent donor–acceptor–radical system. *Nature Chemistry*, 11(11):981–986, Nov 2019.

[12] Charles H. Bennett, Gilles Brassard, Claude Crépeau, Richard Jozsa, Asher Peres, and William K. Wootters. Teleporting an unknown quantum state via dual classical and einstein-podolsky-rosen channels. *Phys. Rev. Lett.*, 70:1895–1899, Mar 1993.

[13] Dik Bouwmeester, Jian-Wei Pan, Klaus Mattle, Manfred Eibl, Harald Weinfurter, and Anton Zeilinger. Experimental quantum teleportation. *Nature*, 390(6660):575–579, Dec 1997.

[14] Samuel L. Braunstein and H. J. Kimble. Teleportation of continuous quantum variables. *Phys. Rev. Lett.*, 80:869–872, Jan 1998.

[15] Rupert Ursin, Thomas Jennewein, Markus Aspelmeyer, Rainer Kaltenbaek, Michael Lindenthal, Philip Walther, and Anton Zeilinger. Quantum teleportation across the danube. *Nature*, 430(7002):849–849, Aug 2004.

[16] Xian-Min Jin, Ji-Gang Ren, Bin Yang, Zhen-Huan Yi, Fei Zhou, Xiao-Fan Xu, Shao-Kai Wang, Dong Yang, Yuan-Feng Hu, Shuo Jiang, Tao Yang, Hao Yin, Kai Chen, Cheng-Zhi Peng, and Jian-Wei Pan. Experimental free-space quantum teleportation. *Nature Photonics*, 4(6):376–381, Jun 2010.

[17] I. Marcikic, H. de Riedmatten, W. Tittel, H. Zbinden, and N. Gisin. Long-distance teleportation of qubits at telecommunication wavelengths. *Nature*, 421(6922):509–513, Jan 2003.

[18] Xi-Lin Wang, Xin-Dong Cai, Zu-En Su, Ming-Cheng Chen, Dian Wu, Li Li, Nai-Le Liu, Chao-Yang Lu, and Jian-Wei Pan. Quantum teleportation of multiple degrees of freedom of a single photon. *Nature*, 518(7540):516–519, Feb 2015.

[19] M. A. Nielsen, E. Knill, and R. Laflamme. Complete quantum teleportation using nuclear magnetic resonance. *Nature*, 396(6706):52–55, Nov 1998.

[20] A. Furusawa, J. L. SÃžrensen, S. L. Braunstein, C. A. Fuchs, H. J. Kimble, and E. S. Polzik. Unconditional quantum teleportation. *Science*, 282(5389):706–709, 1998.

[21] T. C. Zhang, K. W. Goh, C. W. Chou, P. Lodahl, and H. J. Kimble. Quantum teleportation of light beams. *Phys. Rev. A*, 67:033802, Mar 2003.

[22] Jacob F. Sherson, Hanna Krauter, Rasmus K. Olsson, Brian Julsgaard, Klemens Hammerer, Ignacio Cirac, and Eugene S. Polzik. Quantum teleportation between light and matter. *Nature*, 443(7111):557–560, Oct 2006.

[23] M. D. Barrett, J. Chiaverini, T. Schaetz, J. Britton, W. M. Itano, J. D. Jost, E. Knill, C. Langer, D. Leibfried, R. Ozeri, and D. J. Wineland. Deterministic quantum teleportation of atomic qubits. *Nature*, 429(6993):737–739, Jun 2004.

[24] Félix Bussières, Christoph Clausen, Alexey Tiranov, Boris Korzh, Varun B. Verma, Sae Woo Nam, Francesco Marsili, Alban Ferrier, Philippe Goldner, Harald Herrmann, Christine Silberhorn, Wolfgang Sohler, Mikael Afzelius, and Nicolas Gisin. Quantum teleportation from a telecom-wavelength photon to a solid-state quantum memory. *Nature Photonics*, 8(10):775–778, Oct 2014.

[25] S. Pirandola, J. Eisert, C. Weedbrook, A. Furusawa, and S. L. Braunstein. Advances in quantum teleportation. *Nature Photonics*, 9(10):641–652, Oct 2015.

[26] Xiao-Min Hu, Yu Guo, Bi-Heng Liu, Chuan-Feng Li, and Guang-Can Guo. Progress in quantum teleportation. *Nature Reviews Physics*, 5(6):339–353, Jun 2023.

[27] K. M. Salikhov, J. H. Golbeck, and D. Stehlik. Quantum teleportation across a biological membrane by means of correlated spin pair dynamics in photosynthetic reaction centers. *Applied Magnetic Resonance*, 31(1):237–252, Mar 2007.

[28] J. J. Sakurai and Jim Napolitano. *Modern Quantum Mechanic*. Pearson, 2nd edition, 2010.

[29] David S. Sholl and Janice A. Steckel. *Density Functional Theory: A Practical Introduction*. Wiley-Interscience, 1st edition, 2009.

[30] Attila Szabo and Neil S. Ostlund. *Modern Quantum Chemistry: Introduction to Advanced Electronic Structure Theory*. Dover Publications, Reprint Edition, 1996.

[31] Eberhard K. U. Gross Reiner M. Dreizler. *Density Functional Theory: An Approach to the Quantum Many-Body Problem*. Springer Berlin, 1st edition, 2012.

[32] L. Wilk S. H. Vosko and M. Nusair. Accurate spin-dependent electron liquid correlation energies for local spin density calculations: a critical analysis. *Canadian Journal of Physics*, 58:1200–1211, 1980.

[33] J. P. Perdew and Alex Zunger. Self-interaction correction to density functional approximations for many-electron systems. *Phys. Rev. B*, 23:5048–5079, 1981.

[34] Lee A. Cole and J. P. Perdew. Calculated electron affnities of the elements. *Phys. Rev. A*, 25:1265–1271, 1982.

[35] John P. Perdew and Yue Wang. Accurate and simple analytic representation of the electron-gas correlation energy. *Phys. Rev. B*, 45:13244–13249, 1992.

[36] Fernando Nogueira Angel Rubio Kieron Burke Eberhard K. U. Gross Miguel A.L. Marques, Carsten A. Ullrich. *Time-Dependent Density Functional Theory*. Springer Berlin, 1st edition, 2006.

[37] Fernando M.S. Nogueira E.K.U. Gross Angel Rubio Miguel A.L. Marques, Neepa T. Maitra. *Fundamentals of Time-Dependent Density Functional Theory*. Springer Berlin, 1st edition, 2012.

[38] K. M. Martins M. A. Rohrdanz and J. M. Herbert. A long-range-corrected density functional that performs well for both ground-state properties and time-dependent density functional theory excitation energies, including charge-transfer excited states. *J. Chem. Phys.*, 130:054112, 2009.

[39] E. Livshits R. Baer and U. Salzner. Tuned range-separated hybrids in density functional theory. *Annu. Rev. Phys. Chem*, 61:85, 2010.

[40] E. Livshits and R. Baer. A well-tempered density functional theory of electrons in molecules. *Phys. Chem. Chem. Phys*, 9:2932, 2007.

[41] U. Salzner and R. Baer. Koopmansâ springs to life. *J. Chem. Phys.*, 131:231101, 2009.

[42] Tunna Baruah and Mark R. Pederson. Dft calculations on charge-transfer states of a carotenoid-porphyrin-c60 molecular triad. *J. Chem. Theory Comput.*, 5:834â843, 2009.

[43] Mark R. Pederson and Koblar A. Jackson. Variational mesh for quantum-mechanical simulations. *Phys. Rev. B*, 41:7453–7461, Apr 1990.

[44] Koblar Jackson and Mark R. Pederson. Accurate forces in a local-orbital approach to the local-density approximation. *Phys. Rev. B*, 42:3276–3281, Aug 1990.

[45] Dirk Porezag and Mark R. Pederson. Optimization of gaussian basis sets for density-functional calculations. *Phys. Rev. A*, 60:2840–2847, Oct 1999.

[46] M.R. Pederson, D.V. Porezag, J. Kortus, and D.C. Patton. Strategies for massively parallel local-orbital-based electronic structure methods. *Phys. Status Solidi (b)*, 217(1):197–218, 2000.

[47] Tunna Baruah and Mark R. Pederson. Dft calculations on charge-transfer states of a carotenoid-porphyrin-c60 molecular triad. *Journal of Chemical Theory and Computation*, 5(4):834–843, 2009. PMID: 26609590.

[48] Tunna Baruah, Marco Olguin, and Rajendra R. Zope. Charge transfer excited state energies by perturbative delta self consistent field method. *The Journal of Chemical Physics*, 137(8):084316, 08 2012.

[49] Yihan Shao, Zhengting Gan, Evgeny Epifanovsky, Andrew T.B. Gilbert, Michael Wormit, Joerg Kussmann, Adrian W. Lange, Andrew Behn, Jia Deng, Xintian Feng, Debashree Ghosh, Matthew Goldey, Paul R. Horn, Leif D. Jacobson, Ilya Kaliman, Rustam Z. Khaliullin, Tomasz KuÅ, Arie Landau, Jie Liu, Emil I. Proynov, Young Min Rhee, Ryan M. Richard, Mary A. Rohrdanz, Ryan P. Steele, Eric J. Sundstrom, H. Lee Woodcock III, Paul M. Zimmerman, Dmitry Zuev, Ben Albrecht, Ethan Alguire, Brian Austin, Gregory J. O. Beran, Yves A. Bernard, Eric Berquist, Kai Brandhorst, Ksenia B. Bravaya, Shawn T. Brown, David Casanova, Chun-Min Chang, Yunqing Chen, Siu Hung Chien, Kristina D. Closser, Deborah L. Crittenden, Michael Diedenhofen, Robert A. DiStasio Jr., Hainam Do, Anthony D. Dutoi, Richard G. Edgar, Shervin Fatehi, Laszlo Fusti-Molnar, An Ghysels, Anna Golubeva-Zadorozhnaya, Joseph Gomes, Magnus W.D. Hanson-Heine, Philipp H.P. Harbach, Andreas W. Hauser, Edward G. Hohenstein, Zachary C. Holden, Thomas-C. Jagau, Hyunjun Ji, Benjamin Kaduk, Kirill Khistyaev, Jaehoon Kim, Jihan Kim, Rollin A. King, Phil Klunzinger, Dmytro Kosenkov, Tim Kowalczyk, Caroline M. Krauter, Ka Un Lao, AdÃšle D. Laurent, Keith V. Lawler, Sergey V. Levchenko, Ching Yeh Lin, Fenglai Liu, Ester Livshits, Rohini C. Lochan, Arne Luenser, Prashant Manohar, Samuel F. Manzer, Shan-Ping Mao, Narbe Mardirossian, Aleksandr V. Marenich, Simon A. Maurer, Nicholas J. Mayhall, Eric Neuscamman, C. Melania Oana, Roberto Olivares-Amaya, Darragh P. OâNeill, John A. Parkhill, Trilisa M. Perrine, Roberto Peverati, Alexander Prociuk, Dirk R. Rehn, Edina Rosta, Nicholas J.

Russ, Shaama M. Sharada, Sandeep Sharma, David W. Small, Alexander Sodt, Tamar Stein, David StÃŒck, Yu-Chuan Su, Alex J.W. Thom, Takashi Tsuchimochi, Vitalii Vanovschi, Leslie Vogt, Oleg Vydrov, Tao Wang, Mark A. Watson, Jan Wenzel, Alec White, Christopher F. Williams, Jun Yang, Sina Yeganeh, Shane R. Yost, Zhi-Qiang You, Igor Ying Zhang, Xing Zhang, Yan Zhao, Bernard R. Brooks, Garnet K.L. Chan, Daniel M. Chipman, Christopher J. Cramer, William A. Goddard III, Mark S. Gordon, Warren J. Hehre, Andreas Klamt, Henry F. Schaefer III, Michael W. Schmidt, C. David Sherrill, Donald G. Truhlar, Arieh Warshel, Xin Xu, AlÃ¡n Aspuru-Guzik, Roi Baer, Alexis T. Bell, Nicholas A. Besley, Jeng-Da Chai, Andreas Dreuw, Barry D. Dunietz, Thomas R. Furlani, Steven R. Gwaltney, Chao-Ping Hsu, Yousung Jung, Jing Kong, Daniel S. Lambrecht, WanZhen Liang, Christian Ochsenfeld, Vitaly A. Rassolov, Lyudmila V. Slipchenko, Joseph E. Subotnik, Troy Van Voorhis, John M. Herbert, Anna I. Krylov, Peter M.W. Gill, and Martin Head-Gordon. Advances in molecular quantum chemistry contained in the q-chem 4 program package. *Molecular Physics*, 113(2):184–215, 2015.

Appendix A

Analytical Integrals

$$
\begin{aligned}
-\left\langle \Psi_i^{model} \left| V_{model}^{i} \right| \Psi_i^{model} \right\rangle &= \int d^3 r \Psi_i^{*model} V_i e^{-\beta_i (r-C_i)^2} \Psi_i^{model} \\
&= V_i \sum_{n_x n_y n_z}^{N} \sum_{p_x p_y p_z}^{N} \psi_{n_x n_y n_z} \psi_{p_x p_y p_z} \{ \\
&\times \int dx e^{-(2\alpha+\beta)x^2} x^{\mathrm{nx+px}} \\
&\times \int dy e^{-(2\alpha+\beta)y^2} y^{\mathrm{ny+py}} \\
&\times \int dz e^{-(2\alpha+\beta)z^2} z^{\mathrm{nz+pz}} \} \\
&= V_i \sum_{n_x n_y n_z}^{N} \sum_{mjk}^{N} \psi_{n_x n_y n_z} \psi_{mjk} \{ \\
&\times \frac{1}{8} \left((-1)^{\mathrm{nx+px}} + 1 \right) \left((-1)^{\mathrm{ny+py}} + 1 \right) \left((-1)^{\mathrm{nz+pz}} + 1 \right) \\
&\times \Gamma \left(\frac{1}{2} (\mathrm{nx} + \mathrm{px} + 1) \right) \Gamma \left(\frac{1}{2} (\mathrm{ny} + \mathrm{py} + 1) \right) \\
&\times \Gamma \left(\frac{1}{2} (\mathrm{nz} + \mathrm{pz} + 1) \right) \\
&\times (2\alpha + \beta)^{\frac{1}{2}(-\mathrm{nx}-\mathrm{px}-1)+\frac{1}{2}(-\mathrm{ny}-\mathrm{py}-1)+\frac{1}{2}(-\mathrm{nz}-\mathrm{pz}-1)} \}
\end{aligned}
\tag{A.1}
$$

$$
\begin{aligned}
\left\langle \Psi_i^{model} \mid \Psi_i^{model} \right\rangle &= \int d^3 r \Psi_i^{*model} \Psi_i^{model} \\
&= \sum_{n_x n_y n_z}^{N} \sum_{p_x p_y p_z}^{N} \psi_{n_x n_y n_z} \psi_{p_x p_y p_z} \{ \\
&\times \int dx e^{-2\alpha x^2} x^{\mathrm{nx+px}} \\
&\times \int dy e^{-2\alpha y^2} y^{\mathrm{ny+py}} \\
&\times \int dz e^{-2\alpha z^2} z^{\mathrm{nz+pz}} \} \\
&= \sum_{n_x n_y n_z}^{N} \sum_{mjk}^{N} \psi_{n_x n_y n_z} \psi_{mjk} \{ \\
&\times \left((-1)^{\mathrm{nx+px}} + 1 \right) \left((-1)^{\mathrm{ny+py}} + 1 \right) \left((-1)^{\mathrm{nz+pz}} + 1 \right) \\
&\times \Gamma \left(\frac{1}{2} (\mathrm{nx} + \mathrm{px} + 1) \right) \Gamma \left(\frac{1}{2} (\mathrm{ny} + \mathrm{py} + 1) \right) \\
&\times \Gamma \left(\frac{1}{2} (\mathrm{nz} + \mathrm{pz} + 1) \right) \\
&\times 2^{\frac{1}{2}(-\mathrm{nx}-\mathrm{px}-3)+\frac{1}{2}(-\mathrm{ny}-\mathrm{py}-3)+\frac{1}{2}(-\mathrm{nz}-\mathrm{pz}-3)} \\
&\times \alpha^{\frac{1}{2}(-\mathrm{nx}-\mathrm{px}-1)+\frac{1}{2}(-\mathrm{ny}-\mathrm{py}-1)+\frac{1}{2}(-\mathrm{nz}-\mathrm{pz}-1)} \}
\end{aligned}
\tag{A.2}
$$

$$
\begin{aligned}
-\left\langle \Psi_i^{model} \left| T^i_{model} \right| \Psi_i^{model} \right\rangle &= \int d^3r \Psi_i^{*model} \frac{\nabla_i^2}{2m_i} \Psi_i^{model} \\
&= \frac{1}{2m_i} \sum_{n_x n_y n_z}^{N} \sum_{mjk}^{N} \psi_{n_x n_y n_z} \psi_{mjk} \{ \int dy e^{-2\alpha y^2} y^{j+\mathrm{ny}} \int dz e^{-2\alpha z^2} z^{k+\mathrm{nz}} \\
&\times \int dx e^{-2\alpha x^2} \left(-m \left(4\alpha x^2 + 1 \right) + 2\alpha x^2 \left(2\alpha x^2 - 1 \right) + m^2 \right) x^{m+\mathrm{nx}-2} \\
&+ \int dy e^{-2\alpha y^2} \left(-j \left(4\alpha y^2 + 1 \right) + 2\alpha y^2 \left(2\alpha y^2 - 1 \right) + j^2 \right) y^{j+\mathrm{ny}-2} \\
&\times \int dx e^{-2\alpha x^2} x^{m+\mathrm{nx}} \int dz e^{-2\alpha z^2} z^{k+\mathrm{nz}} \\
&+ \int dz e^{-2\alpha z^2} \left(-k \left(4\alpha z^2 + 1 \right) + 2\alpha z^2 \left(2\alpha z^2 - 1 \right) + k^2 \right) z^{k+\mathrm{nz}-2} \\
&\times \int dx e^{-2\alpha x^2} x^{m+\mathrm{nx}} \int dy e^{-2\alpha z^2} z^{k+\mathrm{nz}} \} \\
&= \frac{1}{2m_i} \sum_{n_x n_y n_z}^{N} \sum_{mjk}^{N} \psi_{n_x n_y n_z} \psi_{mjk} \{ \\
&\times \left((-1)^{j+\mathrm{ny}} + 1 \right) \left(j^2 - 2j(\mathrm{ny}+1) + (\mathrm{ny}-1)^2 \right) \left((-1)^{k+\mathrm{nz}} + 1 \right) \left((-1)^{m+\mathrm{nx}} + 1 \right) \\
&\times \Gamma \left(\frac{1}{2}(j + \mathrm{ny} - 1.) \right) \Gamma \left(\frac{1}{2}(k + \mathrm{nz} + 1) \right) \Gamma \left(\frac{1}{2}(m + \mathrm{nx} + 1) \right) \\
&\times 2^{\frac{1}{2}(-j-\mathrm{ny}-5)+\frac{1}{2}(-k-\mathrm{nz}-3)+\frac{1}{2}(-m-\mathrm{nx}-3)} \\
&\times \alpha^{\frac{1}{2}(-j-\mathrm{ny}+1)+\frac{1}{2}(-k-\mathrm{nz}-1)+\frac{1}{2}(-m-\mathrm{nx}-1)} \\
&+ \left((-1)^{j+\mathrm{ny}} + 1 \right) \left((-1)^{k+\mathrm{nz}} + 1 \right) \left(k^2 - 2k(\mathrm{nz}+1) + (\mathrm{nz}-1)^2 \right) \left((-1)^{m+\mathrm{nx}} + 1 \right) \\
&\times \Gamma \left(\frac{1}{2}(j + \mathrm{ny} + 1) \right) \Gamma \left(\frac{1}{2}(k + \mathrm{nz} - 1.) \right) \Gamma \left(\frac{1}{2}(m + \mathrm{nx} + 1) \right) \\
&\times 2^{\frac{1}{2}(-j-\mathrm{ny}-3)+\frac{1}{2}(-k-\mathrm{nz}-5)+\frac{1}{2}(-m-\mathrm{nx}-3)} \\
&\times \alpha^{\frac{1}{2}(-j-\mathrm{ny}-1)+\frac{1}{2}(-k-\mathrm{nz}+1)+\frac{1}{2}(-m-\mathrm{nx}-1)} \\
&+ \left((-1)^{j+\mathrm{ny}} + 1 \right) \left((-1)^{k+\mathrm{nz}} + 1 \right) \left((-1)^{m+\mathrm{nx}} + 1 \right) \left(m^2 - 2m(\mathrm{nx}+1) + (\mathrm{nx}-1)^2 \right) \\
&\times \Gamma \left(\frac{1}{2}(j + \mathrm{ny} + 1) \right) \Gamma \left(\frac{1}{2}(k + \mathrm{nz} + 1) \right) \Gamma \left(\frac{1}{2}(m + \mathrm{nx} - 1.) \right) \\
&\times 2^{\frac{1}{2}(-j-\mathrm{ny}-3)+\frac{1}{2}(-k-\mathrm{nz}-3)+\frac{1}{2}(-m-\mathrm{nx}-5)} \\
&\times \alpha^{\frac{1}{2}(-j-\mathrm{ny}-1)+\frac{1}{2}(-k-\mathrm{nz}-1)+\frac{1}{2}(-m-\mathrm{nx}+1)} \} \quad \text{(A.3)}
\end{aligned}
$$

Appendix B

Optimized Parameters

Table B.1: Optimized Parameters

Parameter	C1:Donor		C2:Acceptor		C3:Radical	
	HOMO	LUMO	HOMO	LUMO	HOMO	LUMO
α	0.19	0.14	0.38	0.18	0.12	0.15
β	0.63	0.44	1.75	1.68	0.62	0.57
V	68497.48	22709.46	42877.84	92676.84	38217.78	58878.95
m	0.27	0.22	0.54	0.29	0.18	0.25
μ_{100}				-1.64		
μ_{010}				-1.03		
μ_{001}				-0.66		
μ_{200}	20.37				-14.66	-2.66
μ_{110}	3.85				-6.13	-6.50
μ_{020}	20.54				-32.56	-2.66
μ_{101}	4.38				-22.41	-6.34
μ_{011}	2.68				-46.05	-6.29
μ_{002}	16.83				-0.56	-2.65

Table B.1 Continued: Optimized Parameters.

Parameter	C1:Donor		C2:Acceptor		C3:Radical	
	HOMO	LUMO	HOMO	LUMO	HOMO	LUMO
μ_{300}		-686.57	-12.70	2.62	0	-2.37
μ_{210}		-135.64	14.09	-1.14	0	1.16
μ_{120}		-176.23	-12.37	2.31	0	-5.49
μ_{030}		-150.33	-1.093	2.57	0	-1.96
μ_{201}		207.60	-5.81	2.56	0	-8.89
μ_{111}		-19.28	0.46	0.39	0	-1.49
μ_{021}		76.04	-11.58	2.00	0	1.00
μ_{102}		-132.40	1.81	0.32	0	-5.33
μ_{012}		-68.34	-4.10	0.05	0	-4.80
μ_{003}		194.31	-3.44	-0.11	0	-1.11

Table B.1 Continued: Optimized Parameters.

Parameter	C1:Donor		C2:Acceptor		C3:Radical	
	HOMO	LUMO	HOMO	LUMO	HOMO	LUMO
μ_{400}	2.55				4.51	
μ_{310}	-10.49				1.58	
μ_{220}	-2.58				14.40	
μ_{130}	-2.53				1.03	
μ_{040}	10.47				9.85	
μ_{301}	-5.52				7.87	
μ_{211}	-7.14				15.44	
μ_{121}	-1.40				7.83	
μ_{031}	-14.46				16.42	
μ_{202}	-1.35				4.28	
μ_{112}	-2.62				5.32	
μ_{022}	-13.63				10.73	
μ_{103}	-5.24				5.59	
μ_{013}	-38.09				11.45	
μ_{004}	-65.58				-0.33	

Table B.1 Continued: Optimized Parameters.

Parameter	C1:Donor		C2:Acceptor		C3:Radical	
	HOMO	LUMO	HOMO	LUMO	HOMO	LUMO
μ_{500}		210.02	5.35			6.05
μ_{410}		452.95	-3.05			-7.37
μ_{320}		133.91	12.36			3.98
μ_{230}		32.36	-7.77			4.29
μ_{140}		-81.55	9.47			-2.48
μ_{050}		21.56	0.11			4.42
μ_{401}		-296.75	3.04			1.10
μ_{311}		-296.14	4.14			-4.10
μ_{221}		15.57	5.49			-1.41
μ_{131}		-116.69	5.93			-6.52
μ_{041}		57.40	3.53			1.08
μ_{302}		221.71	6.62			6.44
μ_{212}		52.42	-0.99			3.58
μ_{122}		14.22	6.50			2.73
μ_{032}		-3.40	3.10			1.34
μ_{203}		-133.53	3.60			1.78
μ_{113}		-134.93	2.44			2.97
μ_{023}		21.64	5.04			3.51
μ_{104}		149.97	2.48			1.06
μ_{014}		-6.39	1.73			2.38
μ_{005}		-51.39	1.12			7.67

Table B.1 Continued: Optimized Parameters.

Parameter	C1:Donor		C2:Acceptor		C3:Radical	
	HOMO	LUMO	HOMO	LUMO	HOMO	LUMO
μ_{600}	-2.77					
μ_{510}	-7.52					
μ_{420}	6.99					
μ_{330}	1.12					
μ_{240}	-13.81					
μ_{150}	-0.02					
μ_{060}	0.10					
μ_{501}	3.93					
μ_{411}	1.99					
μ_{321}	9.54					
μ_{231}	4.15					
μ_{141}	1.13					
μ_{051}	2.13					

Table B.1 Continued: Optimized Parameters.

Parameter	C1:Donor		C2:Acceptor		C3:Radical	
	HOMO	LUMO	HOMO	LUMO	HOMO	LUMO
μ_{402}	1.36					
μ_{312}	3.087					
μ_{222}	5.64					
μ_{132}	13.16					
μ_{042}	-15.3					
μ_{303}	0.26					
μ_{213}	-4.83					
μ_{123}	17.57					
μ_{033}	5.20					
μ_{204}	5.53					
μ_{114}	8.13					
μ_{024}	50.02					
μ_{105}	3.20					
μ_{015}	16.91					
μ_{006}	5.15					

Curriculum Vitae

Pedro Ulises Medina Gonzalez attended the Universidad Autonoma de Ciudad Juarez, graduating in 2020 with a bachelor of science in engineering of physics. During this time, He published a paper in the journal physical review A titled "Heat flow reversal in a trapped ion simulator" alongside Drs. Ramos and Rodriguez-lara from Instituto Tecnologico y de Estudios Superiores de Monterrey.

In the spring of 2021, he entered the Graduate School of The University of Texas at El Paso to pursue a master's degree in physics. During this time, he worked as a Teaching Assistant and Joined Drs. Baruah and Zope Electronic Structure Laboratory.

Contact information: pumedinagon@miners.utep.edu